

Observations of single-pass ion cyclotron heating in a trans-sonic flowing plasma

E. A. Bering III,^{1,a)} F. R. Chang Díaz,^{2,b)} J. P. Squire,^{2,b)} T. W. Glover,² M. D. Carter,^{2,b)} G. E. McCaskill,² B. W. Longmier,^{2,b)} M. S. Brukardt,³ W. J. Chancery,^{4,c)} and V. T. Jacobson^{5,c)}

¹Department of Physics and Department of Electrical and Computer Engineering, University of Houston, Houston, Texas 77204-5005, USA

²Ad Astra Rocket Company, Webster, Texas 77598, USA

³Department of Physics, University of Houston, Houston, Texas 77204, USA

⁴Space Exploration Technologies, McGregor, Texas 76657, USA

⁵Electric Propulsion Laboratory, Inc., Monument, Colorado 80132, USA

(Received 28 December 2009; accepted 23 March 2010; published online 29 April 2010)

The VARIable Specific Impulse Magnetoplasma Rocket (VASIMR[®]) is a high power electric spacecraft propulsion system, capable of I_{sp} /thrust modulation at constant power [F. R. Chang Díaz *et al.*, *Proceedings of the 39th AIAA Aerospace Sciences Meeting and Exhibit*, Reno, NV, 8–11 Jan. 2001]. The VASIMR[®] uses a helicon discharge to generate plasma. This plasma is energized by an rf booster stage that uses left hand polarized slow mode waves launched from the high field side of the ion cyclotron resonance. In the experiments reported in this paper, the booster uses 2–4 MHz waves with up to 50 kW of power. This process is similar to the ion cyclotron heating (ICH) in tokamaks, but in the VASIMR[®] the ions only pass through the resonance region once. The rapid absorption of ion cyclotron waves has been predicted in recent theoretical studies. These theoretical predictions have been supported with several independent measurements in this paper. The single-pass ICH produced a substantial increase in ion velocity. Pitch angle distribution studies showed that this increase took place in the resonance region where the ion cyclotron frequency was roughly equal to the frequency on the injected rf waves. Downstream of the resonance region the perpendicular velocity boost should be converted to axial flow velocity through the conservation of the first adiabatic invariant as the magnetic field decreases in the exhaust region of the VASIMR[®]. This paper will review all of the single-pass ICH ion acceleration data obtained using deuterium in the first VASIMR[®] physics demonstrator machine, the VX-50. During these experiments, the available power to the helicon ionization stage increased from 3 to 20+ kW. The increased plasma density produced increased plasma loading of the ICH coupler. Starting with an initial demonstration of single-pass ion cyclotron acceleration, the experiments demonstrate significant improvements in coupler efficiency and in ion heating efficiency. In deuterium plasma, $\geq 80\%$ efficient absorption of 20 kW of ICH input power was achieved. No clear evidence for power limiting instabilities in the exhaust beam has been observed. © 2010 American Institute of Physics. [doi:10.1063/1.3389205]

I. INTRODUCTION

The exploration of the solar system will be one of the defining scientific tasks of the new century. One of the obvious challenges faced by this enterprise is the scale size of the system under study, 10^8 – 10^{14} m. Over distances on this scale, the mission designer is faced with the choice of accepting multiyear or even decadal mission time lines, paying for enormous investment in rocket propellant compared with useful payload, or finding a way to improve on the performance of today's chemical rockets. For human space flight beyond Earth's orbit, medical, psychological, and logistic considerations all dictate that drastic thruster improvement is the only choice that can be made. Even for robotic missions

beyond Mars, mission time lines of years can be obstacles to success and major cost drivers, meaning that improvements in deep space sustainer engines are of importance to all phases of solar system exploration.¹ Improvement in thruster performance can best be achieved by using an external energy source to accelerate or heat the propellant.^{2,3} This paper will discuss an experimental investigation of the use of ion cyclotron heating (ICH) to provide an efficient method of electrodeless plasma acceleration in the VARIable Specific Impulse Magnetoplasma Rocket (VASIMR[®]) engine.

Research on the VASIMR[®] engine began in the late 1970s, as a spin-off from investigations on magnetic divertors for fusion technology.⁴ A simplified schematic of the engine is shown in Fig. 1. The VASIMR[®] consists of three main sections: a helicon plasma source, an ICH rf booster stage or plasma accelerator, and a magnetic nozzle.^{5–10} Figure 1 shows these three stages integrated with the necessary supporting systems. One key aspect of this concept is its

^{a)}Electronic mail: ebering@mail.uh.edu. URL: <http://www.phys.uh.edu/~ebering/>.

^{b)}Also at Department of Physics, University of Houston.

^{c)}Formerly at Ad Astra Rocket Company.

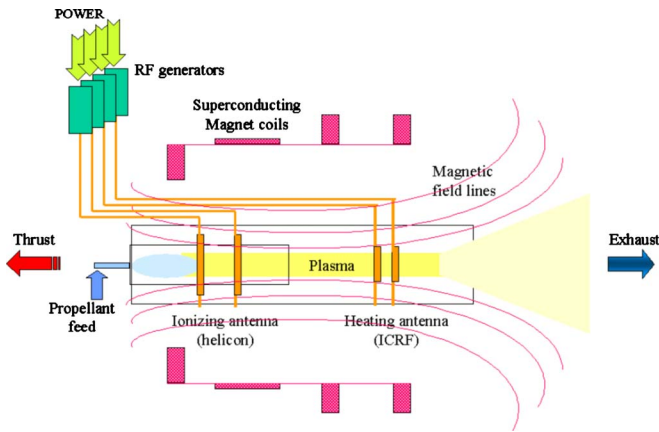


FIG. 1. (Color online) Block diagram of the VASIMR[®] system.

electrodeless design, which makes it suitable for high power density and long component life by reducing plasma erosion and other materials complications. The magnetic field ties the three stages together and, through the magnet assemblies, transmits the exhaust reaction forces that ultimately propel the ship.

The plasma ions are accelerated in the second stage by ICH, a well-known technique, used extensively in magnetic confinement fusion research.^{11–15} An important consideration involves the rapid absorption of ion cyclotron waves by the high-speed plasma flow. This process differs from the familiar ion cyclotron resonance utilized in tokamak fusion plasma as the particles in VASIMR[®] pass under the coupler only once.^{9,16–18} Sufficient ion cyclotron wave (ICW) absorption has nevertheless been predicted by recent theoretical studies.¹⁹

Elimination of a magnetic bottle, a feature in the original VASIMR[®] concept, was motivated by theoretical modeling of single-pass absorption of the ICW on a magnetic field gradient.¹⁹ While the cyclotron heating process in the confined plasma of fusion experiments results in approximately thermalized ion energy distributions, the nonlinear absorption of energy in the single-pass process results in a boost, or displacement of the ion kinetic energy distribution. The ions are ejected through the magnetic nozzle before thermal relaxation occurs.

Natural processes in the auroral region may also exhibit a related form of single-pass ICH. “Ion conic” energetic ion pitch angle distributions are frequently observed in the auroral regions of the Earth’s ionosphere and magnetosphere.^{20–26} It is not relevant to list the entire range of models that have been proposed to account for these observations. Many models propose wave-driven transverse ion acceleration followed by adiabatic upwelling of the distribution.^{27,28} Proposed driver wave modes include current driven electrostatic ion cyclotron (EIC) waves,^{29–31} and electromagnetic ion cyclotron waves (EMIC),^{32–34} among others. Other mechanisms proposed include interaction with an oblique double layer or dc potential structure.^{35,36} The fact that ion conics are commonly found on auroral field lines suggests that transverse ion acceleration is a ubiquitous process in auroral arcs.²⁸ Space-borne observations of narrow-band ion

cyclotron waves with unambiguous spectral peaks near the ion cyclotron frequencies are relatively rare.^{37–45} Most studies have found that the most common wave phenomenon found in association with transverse ion acceleration is broadband extremely low frequency (ELF) noise.^{28,46–49} All of these authors suggest that current driven EIC waves make up some or all of the broadband ELF noise, but they are unable to prove it, even when wavelength measurements are available.^{48,49} The role of inhomogeneities or shear in reducing the threshold for current-driven EIC instability is suggested as one solution to this problem.^{49,50} EMIC waves appear to be associated with transverse ion acceleration 10% of the time.^{28,34}

In addition to the extensive body of work on the heating of magnetic confinement fusion plasmas that was superficially cited above, there is a 30 yr body of theoretical and laboratory work on transverse ion acceleration by current driven EIC modes.^{27,29,36,51,52} All of these experiments have typically used current driven EIC waves, parametric decay of lower hybrid waves, or other mode conversion process to launch the required wave field. Direct injection, which is used in VASIMR[®], requires good plasma coupling to the coupler in order to launch the waves with useful efficiency, as discussed below. Since the magnetospheric simulation experiments have aimed at simulating EIC driven heating and VASIMR[®] uses EMIC waves, these prior results have limited application to the VASIMR[®]. What has been shown of relevance is that acceleration followed by adiabatic folding is a viable mechanism for producing ion conics.^{27,52} However, the field ratios attained were an order of magnitude smaller than used in the VASIMR[®] studies reported here.

VASIMR[®] has a transverse ion acceleration stage or booster that uses EMIC waves, followed by adiabatic expansion. Simultaneous ambipolar acceleration is also observed in the VASIMR[®] exhaust plume that may be interpreted as a large-scale double layer.^{53,54} Thus, VASIMR[®] results may be of interest to proponents of more than one model of ion conic production.

This paper summarizes the data from all of the VX-50 laboratory experiments that have demonstrated single-pass electromagnetic ICH in a trans-sonic flowing deuterium plasma.

II. EXPERIMENT

A. VASIMR[®] engine

The VASIMR[®] engine has three major subsystems, the injection stage, the heating stage and the nozzle.⁸ The VX-50, a laboratory 50 kW proof of concept VASIMR[®] engine, was developed and tested from 1995 to 2006, first by the Advanced Space Propulsion Laboratory at NASA-JSC and subsequently by the Ad Astra Rocket Co.^{55,56} The details of the engine and its design principles have been previously reported.^{9,57} A more specific detailed view of the first physics demonstrator laboratory experiments (VX-10 through VX-50) is shown in Fig. 2. The first stage was a helicon discharge that had been optimized for maximum power efficiency [lowest ionization cost in eV/(electron-ion pair)].^{58–61} The next stage downstream was the rf booster

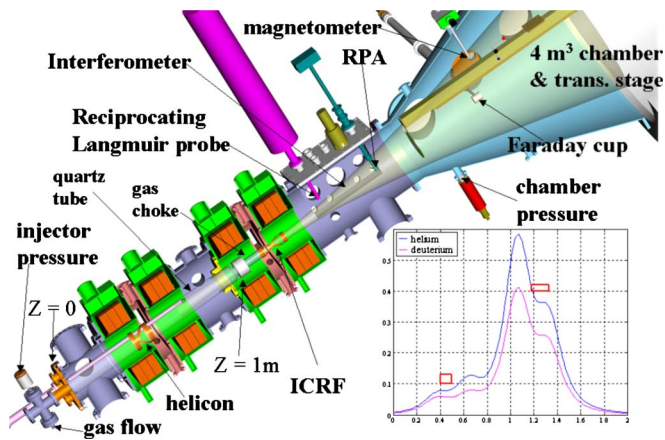


FIG. 2. (Color online) Engineering drawing of the VX-50, showing the major systems and the location of the diagnostic instruments. The RPA used to obtain most of the data in this paper was located, as shown at $z=1.7$ m.

system. Energy was fed to the system in the form of a circularly polarized rf signal tuned to the ion cyclotron frequency. ICH heating was chosen because it transfers energy directly and largely to the ions, which maximizes the efficiency of the engine.^{12,13} The VX-50 did not have a mirror chamber; thus, the ions made one pass through the ICH coupler. The system also featured a two-stage magnetic nozzle, which accelerated ions and electrons by converting their azimuthal energy into directed axial momentum. The detachment of the plume from the magnetic field took place mainly by the loss of adiabaticity and the rapid increase in the local plasma β , defined as the local ratio of the plasma pressure to the magnetic pressure.⁶²

The main VX-50 vacuum chamber was a cylinder 1.8 m long and 35.6 cm in diameter. The VASIMR[®] exhaust flowed through a conical adapter section into a 5 m³ vacuum chamber that served as an exhaust reservoir. The magnetic field was generated by four liquid-nitrogen-cooled 150-turn copper magnets, which could generate a magnetic induction of up to 1.5 T. The high vacuum pumping system consisted of a cryopump and two diffusion pumps with a combined total capacity of 5000 l/s.

1. Helicon discharge

Over the course of the investigations reported here, there were a series of improvements and upgrades to the helicon plasma source.^{63,64} The earliest experiments were performed using a 5 cm diameter “Boswell” type double saddle coupler^{58–60} and 3 kW of rf power. Directionality was provided by use of a magnetic cusp configuration. Over the four year interval spanned by the experiments reported here, the helicon plasma source in the VASIMR[®] engine was incrementally improved in three steps. First, coupler size, connector and power supply improvements raised the available power from 3 kW to 10 kW, still operating with Boswell coupler and a magnetic cusp. The factors limiting the application of rf power to the helicon ionizing discharge had been the power of the 25 MHz transmitter (3 kW), the voltage limits on the vacuum rf feedthrough, the voltage limits of the rf matching network, and the diameter of the discharge. Suc-

cessive steps to 9 cm increased the diameter of the helicon coupler. The helicon rf supply was completely rebuilt. A new high voltage power supply was built, along with a new high power transmitter. A 10 kV rf vacuum feedthrough was obtained and installed, along with a new high voltage matching network. These new components produced helium plasma operating at 10 kW, with ~ 4 times the ion flux achievable at 3 kW. Second, the transmitting coupler was changed from the Boswell configuration to a helical half-twist coupler.^{63,64} Finally, the decision was taken to switch transmitters and power the helicon with a 100 kW transmitter, which operated at 13.5 MHz. A high voltage (30 kV) water-cooled vacuum feedthrough was manufactured to enable full power operation. In all configurations, the vacuum feedthrough and helicon couplers were water cooled and capable of steady state operation.

2. ICH rf booster

The ICH coupler was a helical, double strap quarter-turn coupler configuration. It was polarized to launch left-handed slow mode waves.^{17,65} The first (VX-50) configuration of the rf booster or ICH system used 1.5 kW of 1.5–2.5 MHz left hand polarized slow mode waves launched from the high field, over dense side of the resonance (region 13 of the Clemmow–Mullaly–Allis (CMA) diagram, using the¹⁵ notation). The coupler was uncooled, which typically limited the pulse length to less than 0.5 s. The pulse power was limited by the rf power source to 1.5 kW until 2006, when a 50 kW transmitter was installed. Feedthrough and coupler cooling considerations usually limited the applied rf booster power to ≤ 25 kW.

B. Diagnostics

Available plasma diagnostics included a triple probe, a 70 GHz density interferometer, a bolometer, a television monitor, an H- α photometer, a spectrometer, neutral gas pressure and flow measurements, several gridded energy analyzers (retarding potential analyzer or RPA),^{8,10,66–70} a momentum flux probe, an emission probe, a directional RPA and other diagnostics.⁷¹ Reciprocating Langmuir⁷² and density interferometer were the primary plasma diagnostics. The Langmuir probe measured ion current and temperature profiles and was calibrated by the density interferometer. An array of thermocouples provided a temperature map of the system. The Langmuir probe had four molybdenum tips that were biased as a triple probe, with an extra tip for measuring electrostatic fluctuations.⁷²

1. Retarding potential analyzer

RPA diagnostics were installed to measure the accelerated ions. The University of Houston (UH) VX-50 RPA was a planar ion trap located at $z=1.7$ m in Fig. 2, ~ 40 cm downstream from the plane of the triple and Mach probes, which corresponds to a factor of 8 reduction in the magnetic field strength. The grids were 49.2-wire/cm nickel mesh, spaced 1 mm apart with Macor spacers. The opening aperture was 1 cm in diameter, usually centered on the plasma

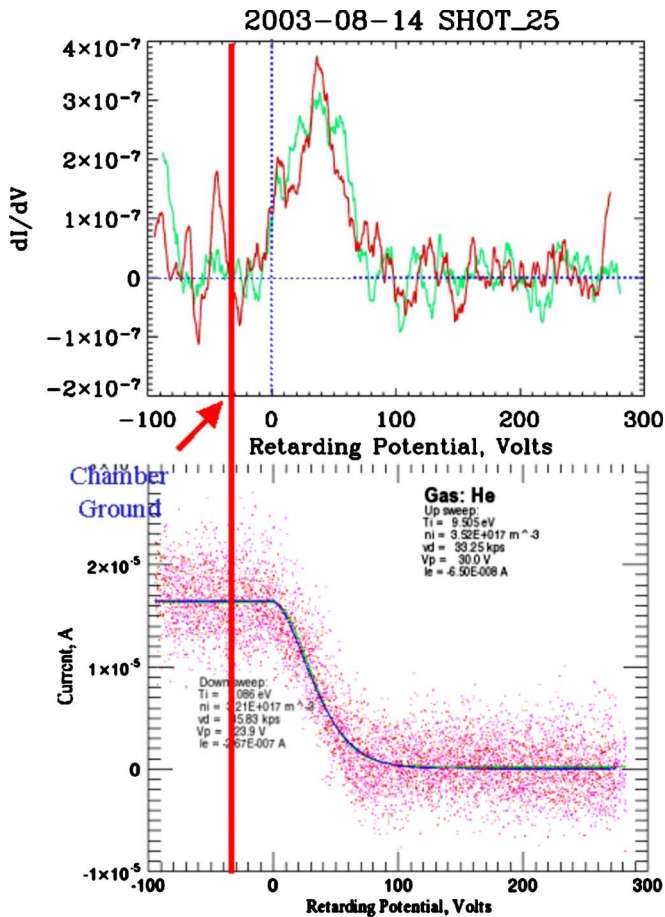


FIG. 3. (Color online) A sample shot of RPA data, showing the relationship of chamber ground to plasma potential.

beam. A four-grid configuration was used, with entrance attenuator, electron suppressor, ion analyzer, and secondary suppressor grids.

The interpretation of RPA output data in terms of ion energy requires an accurate knowledge of plasma potential (V_p). On most RPA plots, the 0 of the retarding potential scale is set to V_p , as shown in Fig. 3, instead of chamber ground. Thus, the sweep scale can be read directly as ion energy in eV. When available, data from an rf compensated swept Langmuir probe provided by Los Alamos National Laboratory (LANL) were used to determine V_p , as shown in Fig. 4 (Ref. 73). When other V_p data were not available, plasma potential was assumed to be the sweep voltage at which dI/dV first significantly exceeded 0, which usually agreed with the LANL probe value within the error bars (± 5 V). In the VX-50, this value was typically $\sim +30$ to $+50$ V with respect to chamber ground. The operator biased the body and entrance aperture of the RPA to this voltage. The ion exhaust parameters are deduced from the raw data by means of least-squares fits of drifting Maxwellians to the current-voltage data.^{67,68,70,74}

In this paper, the RPA data will be presented in several formats, including the voltage derivative of the I-V characteristic, the one-dimensional ion velocity distribution function, a planar cut through the full ion velocity distribution function, and as derived parameters. The dI/dV plots (e.g.,

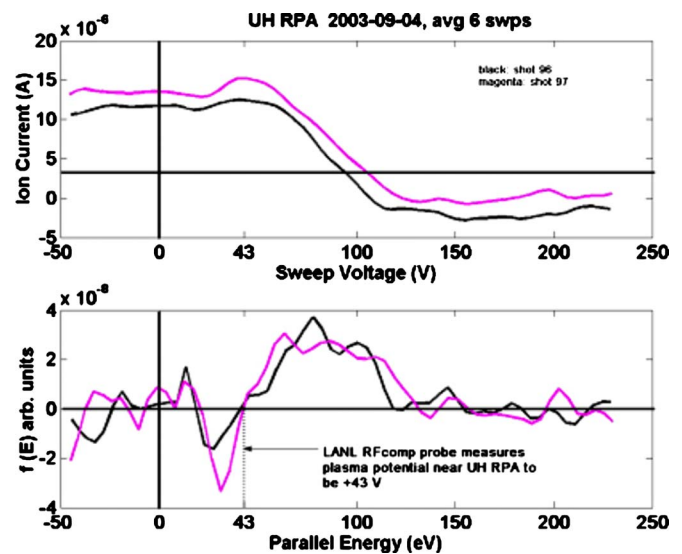


FIG. 4. (Color online) Two sample shots of RPA data with 0 V set to chamber ground, showing the relationship between plasma potential as measured by an rf compensated Langmuir probe and the sweep potential where $dI/dV \approx 0$.

Figs. 3 and 5) show the smoothed, numerically calculated derivative with respect to sweep voltage of the measured RPA current. Sweep voltage zero was usually set to plasma potential found using the methods of the previous paragraph, for ICH off conditions and all other parameters unchanged. Unless stated otherwise, sixteen sweeps per shot of the RPA have been averaged to produce each figure. The presence of features in the dI/dV curves at retarding voltages less than the plasma potential are the result of temporal fluctuations in the ion saturation current, and largely serve to illustrate the risks in taking numerical derivatives of data. The ion velocity distribution functions (e.g., Fig. 6) were found from the dI/dV curves by dividing by the energy and multiplying by a calibration factor.

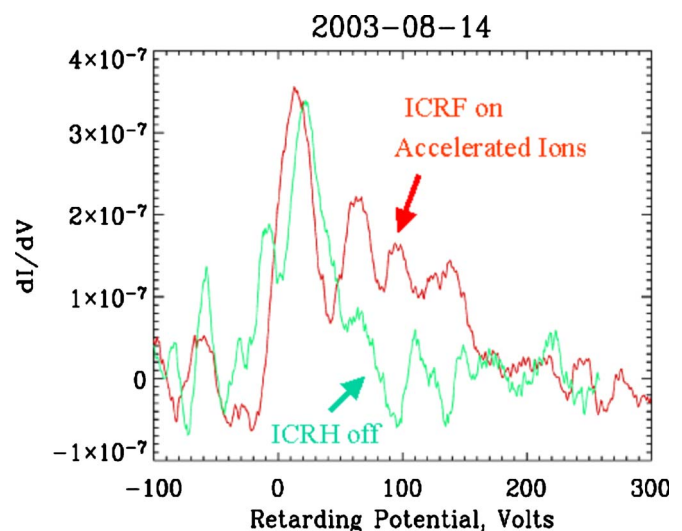


FIG. 5. (Color online) The first derivative of the current-voltage characteristics measured by an RPA with 30° collimation oriented at 10° pitch angle. The lower energy, lighter curve shows a helium shot without ICH, and the upper energy, darker curve shows a helium shot with ICH.

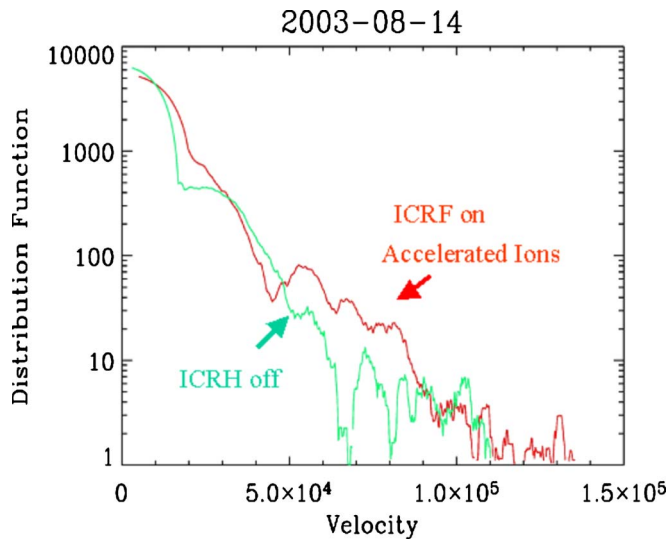


FIG. 6. (Color online) The ion velocity phase space distribution functions inferred from the data shown in Fig. 5.

The RPA I-V characteristic data has been reduced by least-squares fitting the characteristic that would be produced by a drifting Maxwellian to the data. The solid lines on the raw data plots are the results of least-squares fits of drifting Maxwellians to the up and down sweeps. These fits have three parameters: ion density, mean drift speed and the ion temperature in the frame of reference moving with the beam. The temperature is found from these least-squares fits, not from taking the slope of the logarithm of the data. The density is calibrated by comparison to nearby Langmuir probes and is probably best understood as a relative measurement. The temperature and ion drift speed parameters depend most strongly on the accuracy with which the retarding potential is known. The absolute uncertainty of the sweep voltage digitization with respect to chamber ground was a few percent when digitizer calibration uncertainty, sweep isolator reduction ratio precision and related parameters are folded in. There are systematic uncertainties associated with the determinations of plasma potential, which are discussed two paragraphs above. Plasma potential as determined above was always subtracted prior to any other analysis.

The full ion velocity phase space distribution function of the ions was obtained by scanning the RPA in pitch angle between otherwise identical shots, assuming cylindrical (gyrotropic) symmetry.^{75,76} The angle step size was 10° for Figs. 10 and 11, and 5° from 0° to 60° and 10° thereafter for Figs. 24, 25, 30, and 31. All of the data in these figures was obtained in the centerline, at $z=1.7$ m in Fig. 2.

An upper limit to rf smearing of the current-voltage characteristic of the RPA was estimated by examining T_i estimates from Maxwellian fits to the data from the coldest plasma shots obtained. The coldest ion temperature observed with ICH off was 0.7 eV observed with a very high gas flow. The coldest ion temperature during an ICH-on shot was ~ 1 eV. It can be argued that these temperatures represent experimental upper limits on the rf contamination of ion temperature estimates.

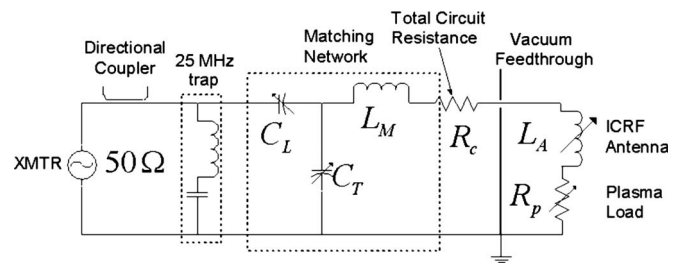


FIG. 7. Circuit diagram of the ICH coupler, indicating how the plasma impedance couples to the circuit.

C. Plasma loading

The VASIMR[®] engine is best suited to high power operation. The critical factor that limits efficiency at low power is the efficiency of the helicon stage and hence the ionization cost.⁷⁷ At high power, the ICH stage is more important and hence ICH coupler loading is more critical. The load impedance of the ICH coupler must be significantly larger than the impedance of the transmission and matching network (see Fig. 7). The cyclotron resonance frequency of deuterium in the available magnetic field was about 2 MHz, which meant that plasma with an $\sim 8-10$ cm diameter was required before reasonable load impedances were obtained.

The following calculation illustrates how plasma loading was determined. The analysis begins with the relationship that

$$\frac{\text{VSWR}_{\text{plasma}}}{\text{VSWR}_{\text{vacuum}}} = \frac{(R_p + R_c)}{R_c}, \quad (1)$$

where VSWR is the voltage standing wave ratio. A network analyzer is used in place of the high power rf transmitter to measure the quality factor (Q_c) of the coupling circuit and to tune the circuit when no plasma is present. With measuring the impedance matching (L_m) and the coupler inductances (L_A), we have

$$R_c = \frac{\omega(L_M + L_A)}{Q_c} \approx 0.24 \Omega \quad (2)$$

and

$$R_p = R_c(\text{VSWR}_{\text{plasma}} - 1). \quad (3)$$

Thus, the coupling efficiency is

$$\eta_A = \frac{R_p}{(R_p + R_c)} = 0.89, \quad (4)$$

and the power radiated into the plasma is estimated as

$$P_{\text{plasma}} = \eta_A P_{\text{ICH}}. \quad (5)$$

The initial deuterium ICH loading data were taken when only 4 kW of helicon power was available. Plasma loading was generally maximum when $f/f_{ci} > 1$. The ICH plasma loading was comparable to the circuit resistance. Helium data showed similar behavior.

Subsequent loading measurements were made using a 20 kW helicon discharge. The measurements showed very good loading, $\sim 2 \Omega$, which implies a corresponding high

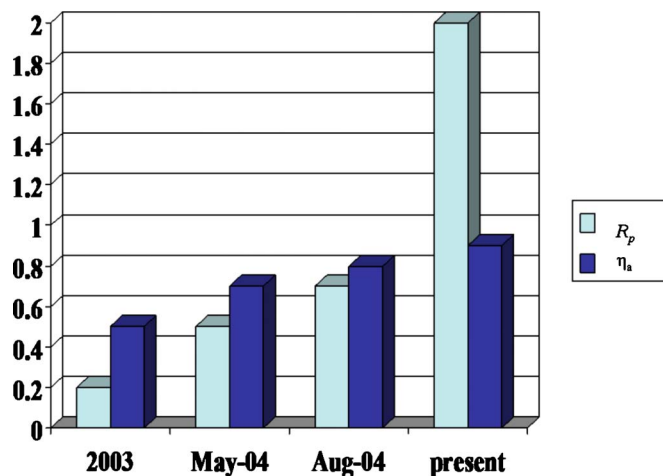


FIG. 8. (Color online) Time history of the plasma loading of the ICH coupler and coupler efficiency. Present refers to the VX-50 in 2005 and 2006.

coupling efficiency, as shown in Fig. 8. This high loading impedance was obtained with a sizable, ~ 1 cm, plasma-coupler gap. Maximum in the loading occurred at $f/f_{ci} = 0.95$, indicating that the coupler was launching a more propagating wave than it was in the low density case.

III. ION CYCLOTRON HEATING

A. Low density discharge, 1.5 kW ICH

Until 2006, the rf booster or ICH system used 1.5 kW of 1.85 MHz left hand polarized slow mode waves launched from the high field, overdense side of the resonance (region 13 of the CMA diagram). An important consideration involves the rapid absorption of ion cyclotron waves by the high-speed plasma flow. This process differs from the familiar ion cyclotron resonance utilized in tokamak fusion plasmas as the particles in VASIMR[®] pass under the coupler only once. Sufficient ICW absorption has nevertheless been predicted by recent theoretical studies. The experiments presented below have supported these theoretical predictions with a number of independent measurements.

The earliest results were obtained with a 3 kW helicon discharge using a Boswell type helicon coupler during the summer of 2003.^{9,10,63–65} The effect of the ICH heating was expected to be an increase in the component of the ion velocity perpendicular to the magnetic field. This increase takes place in the resonance region, i.e., the location where the injected rf wave frequency was equal to the ion cyclotron frequency. Downstream of the resonance, this perpendicular heating was converted into axial flow owing to the requirement that the first adiabatic invariant of the particle motion be conserved as the magnetic field decreased (Figs. 5, 6, and 19). Since the total ion flux was not expected to increase, this axial acceleration should have been accompanied by a density decrease, as shown in Figs. 9 and 18. Furthermore, the particles should have had a pitch angle distribution that does not peak at 0° . Instead, the distribution should have peaked at an angle that maps to a perpendicular pitch angle at resonance (Fig. 10). Therefore a collimated detector oriented along the magnetic field should have observed a decrease in

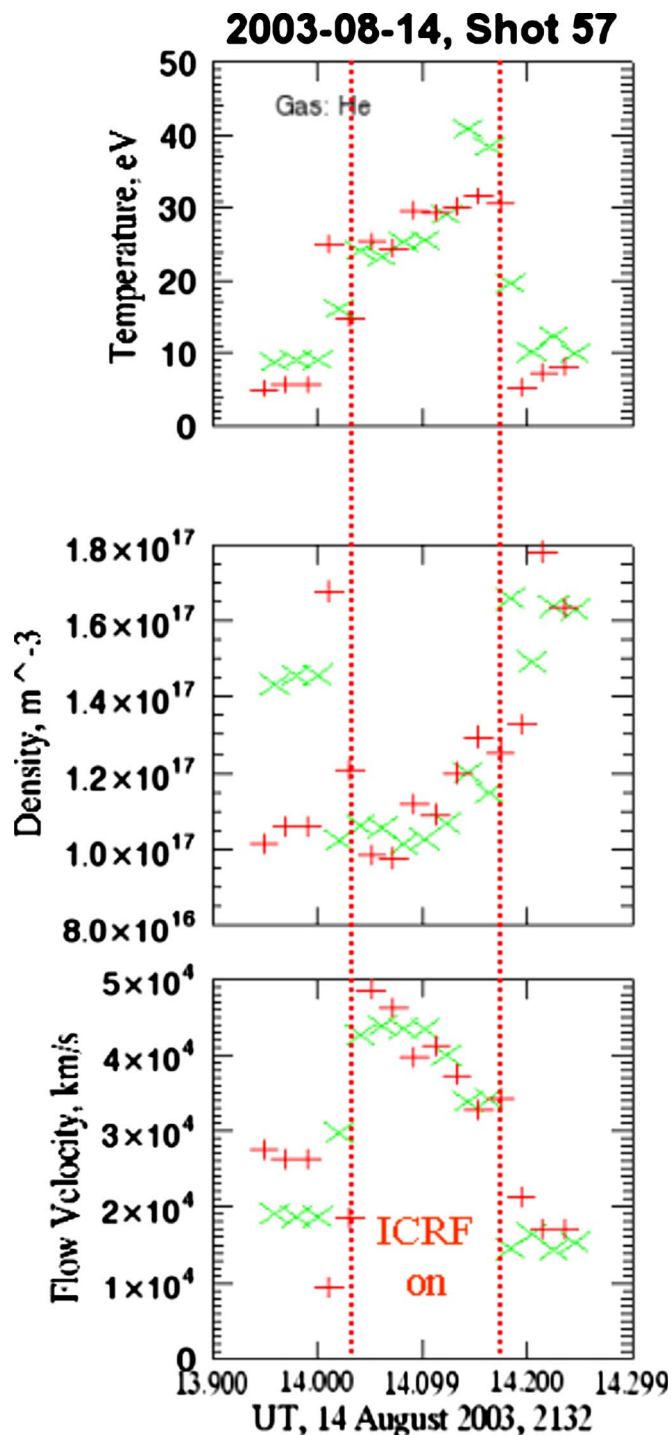


FIG. 9. (Color online) Fit parameters obtained by least-squares fitting a drifting Maxwellian representation to each voltage sweep obtained by the wide angle RPA during a pulsed ICH helium plasma shot. From top to bottom, the panels show ion drift velocity, ion density and ion temperature in the frame of the beam. The pluses and X's show up and down sweeps. The vertical dashed lines show the times when the ICH turned on and off.

total flux and an increase in particle energy. As the acceptance angle of the detector increased, the ion saturation current should have shown an increase when the acceptance cone includes the peak in the pitch angle distribution.

Three RPA configurations were available, tightly (2.5°) collimated, moderately (10°) collimated and effectively uncollimated (30°). The first two configurations were axially

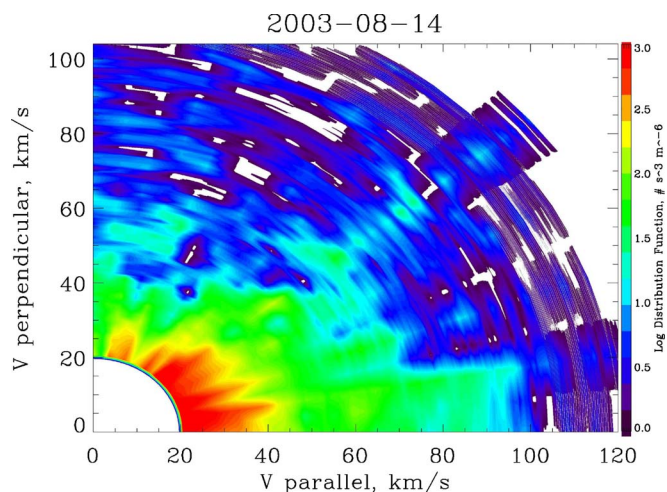


FIG. 10. (Color online) The ion velocity phase space distribution function obtained in a 3 kW helium discharge with 1.5 kW of ICH on. The distribution function grayscale bar scale is logarithmic. Note the intense 60–100 km/s ion jet at 10°-pitch angle.

mounted and could be scanned along the axis of the engine. The third RPA could be rotated to any pitch angle and could be used to obtain three-dimensional pitch angle distributions. Figure 5 shows a comparison of the first derivative of the characteristic curve obtained by the wide aperture RPA during helium plasma shots run with and without ICH. The upper, darker curve shows data taken during the ICH shot. This upper curve shows an elevated multi-peaked section between 50 and 130 eV, where the ion energy distribution was much larger than in the shot where the ICH was off. The energy range where this increase occurred was above the thermal range of the ICH-off ion distribution. Thus, this increase indicated the presence of a population of strongly heated ions.

The presence of what appeared to be a hot component with low drift velocity is attributed to charge exchange with background neutral deuterium molecules. Since the pumping capacity was small relative to the injected gas flow, the background pressure built up to at least 20 μtorr in the 50 cm region between the ICH coupler and the RPA during the period of the discharge when RPA data were taken. Perhaps half the particles were in the accelerated component of the distribution, whereas half remained in (or have been charge exchanged and thermalized back into) the lower energy component of the distribution. The velocity phase space distribution functions corresponding to Fig. 5 are found by dividing by the energy and are shown in Fig. 6. The differences between the two curves appear less dramatic in this logarithmic presentation. Nonetheless, the effect of significant particle heating is apparent.

The dynamic response of the plasma to the ICH energy input was studied by examining the temporal response of the plasma to brief bursts of ICH transmission during individual shots. In order to simplify the plotting task, we have characterized the plasma during each voltage sweep of the retarding potential by least-squares fitting a single component drifting Maxwellian to the RPA data. Figures 5 and 6 make clear that a single Maxwellian is a relatively poor approximation to the data. However, time variations in the inferred parameters do

provide a general illustration of what was happening in the plasma. The term temperature refers, in effect, to the parallel ion temperature in the frame of reference drifting with the ion beam.

Figure 9 shows an example of a time series plot obtained during a single helium shot. From top to bottom the panels show drift velocity, ion density, and ion temperature in the drifting frame. The wide aperture RPA oriented at 5°-pitch angle took these data. Three effects of the ICH are apparent in the figure. Drift speed increased substantially, the density dropped and the temperature increased. All of the effects conform closely to the expected response to ICH. Since, a single drifting Maxwellian is a poor approximation to the actual distribution function, the actual speed attained by the accelerated component is higher than the figure shows.

The full ion velocity phase space distribution function of the ions can be obtained by scanning the RPA in pitch angle, assuming cylindrical (gyrotropic) symmetry.^{75,76} An example of a helium distribution function that was observed during ICH experiments is shown in Fig. 10. During this particular experiment, the ICH transmitter was operated at 1.85 MHz, at a power level of 1500 W. The data show a pronounced enhancement or jet of ions with $v > 60$ km/s at 10° pitch angle. Although not particularly evident in the figure, detailed examination of the data show a depletion of ions with lower velocities and pitch angles.

As shown in Fig. 2, the magnetic field intensity decreased rapidly with axial distance downstream away from the resonance region. At the location of the RPA, the magnetic field strength was down by a factor of ~ 40 from the value at the cyclotron resonance point. In a region like this, the effects of conservation of the first adiabatic invariant dominate ion dynamics. Conservation of the first invariant forces particles to lower pitch angles as the magnetic field strength drops. This mechanism is the basis for the magnetic nozzle that makes the VASIMR[®] an attractive design concept in the first place. A particle's pitch angle is given by

$$\theta = \arcsin(\sin(\theta_0)\sqrt{B/B_0}). \quad (6)$$

A particle with a pitch angle of 90° at the resonance region will have a pitch angle of 10° at the location of the RPA. Thus all of the particles detected at $\theta > 10^\circ$ are either artifacts of the lack of collimation in the RPA or particles that have been scattered or charge exchanged.

The effect of ICH on the exhaust plasma was illustrated by subtracting the “ICH off” distribution function from the “ICH on” distribution function and mapping the result back to the resonance region (Fig. 11). There is a clear depletion of low energy ions and a significant enhancement of ions with perpendicular speeds $v_\perp > 60$ km/s.

The data in Figs. 5–11 indicate that the high remaining neutral background pressure in the VX-50 VASIMR[®] test chamber produced a substantial amount of resonant charge exchange and scattering between the ICH coupler and the RPA location. This problem was much more acute when using helium than when using gasses such as deuterium that have a molecular configuration as neutral gasses. The result of the charge exchange was a pronounced “two-bump” distribution that was not well modeled by a single drifting

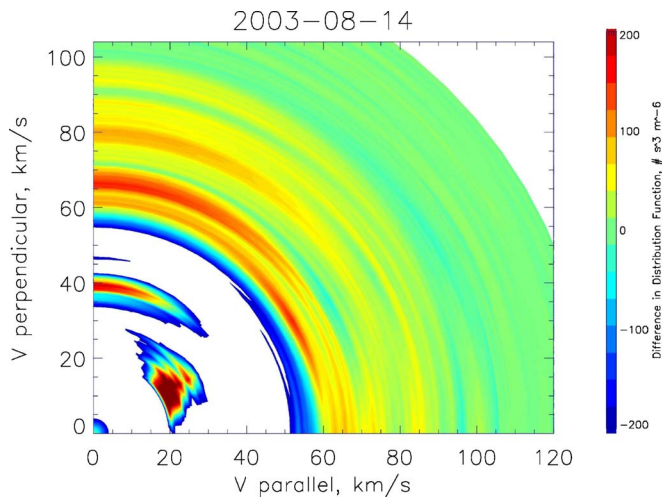


FIG. 11. (Color online) The difference in helium velocity phase space distribution functions between ICH-on and ICH-off conditions. The distribution function grayscale bar scale is linear. The distribution has been mapped back to the location of cyclotron resonance using conservation of the first adiabatic invariant. The perpendicular heating effect of the ICH shows up as the intense features at perpendicular velocities of 60–100 km/s.

Maxwellian.^{78–81} The data in Fig. 6 strongly suggested using a bi-Maxwellian model consisting of a hot, slow component and a fast component that has a low temperature in the moving frame. An example of a bi-Maxwellian fit is shown in Fig. 12.

1. ICH power scans

The bi-Maxwellian model analysis was used to interpret the results of a series of shots that scanned the ICH power input at 0–1500 W. These results are presented in Fig. 13. These results provide convincing evidence of single-pass

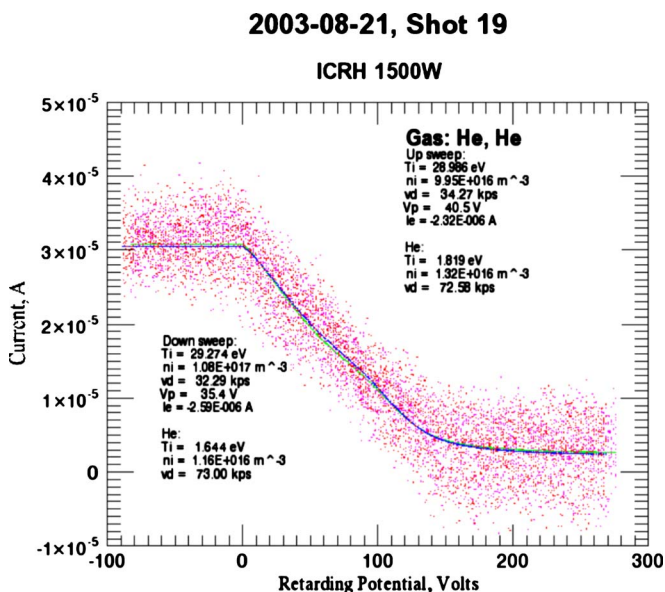


FIG. 12. (Color online) Raw RPA anode current plotted as a current-voltage characteristic. Data were obtained during a low density ICH-on helium shot. Solid lines show least-squares fits of drifting bi-Maxwellian representations, showing that the data can be modeled as the sum of a hot, slow component and a cold, fast component.

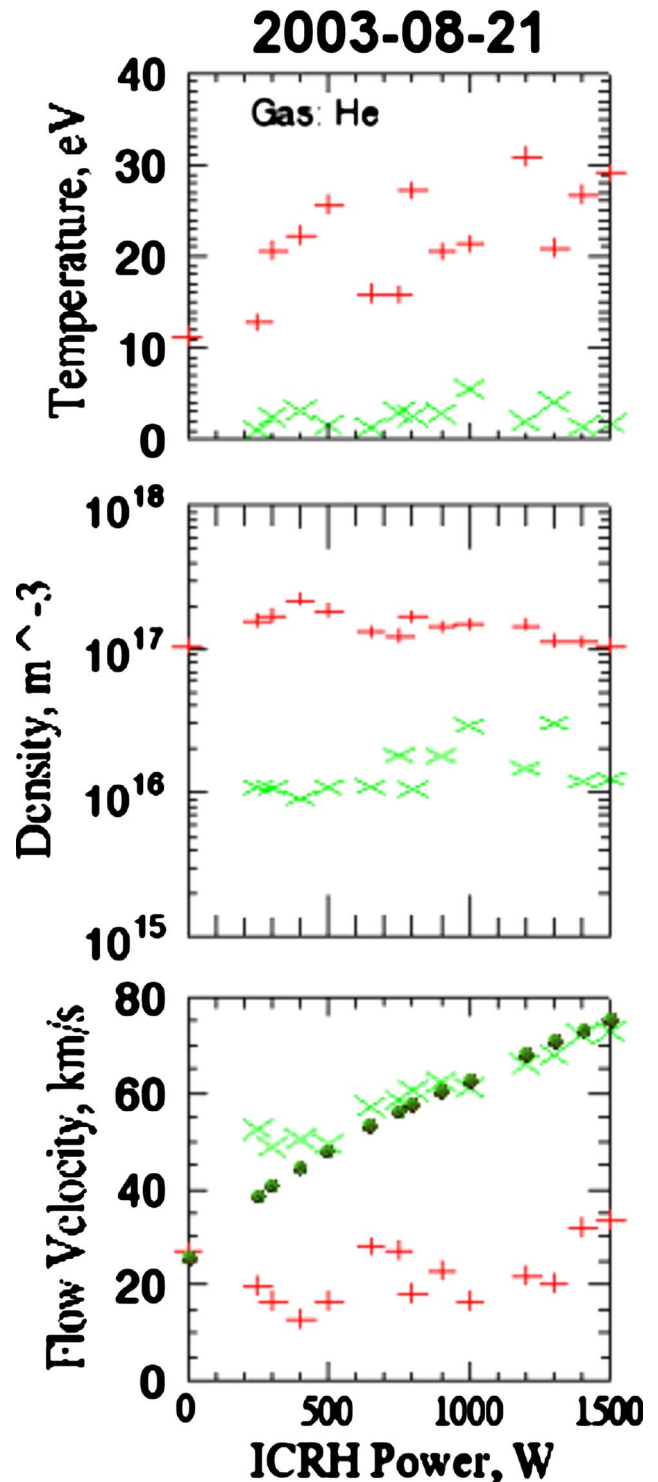


FIG. 13. (Color online) Fit parameters obtained by least-squares fitting drifting bi-Maxwellian representations to the RPA data obtained during a scan of ICH transmitter power. From top to bottom, the panels show ion drift velocity, ion density and ion temperature in the frame of the beam. The plusses show the slow, hot component. The X's show the fast, cold accelerated component. The round dots show the flow velocity expected for an energization rate of 70 eV/ion/kW of transmitted rf power.

ICH heating. The top panel shows that the accelerated beam had a low temperature in its reference frame, consistent with the expected output temperature of the helicon discharge. The temperature of the hot component was noisy. Generally

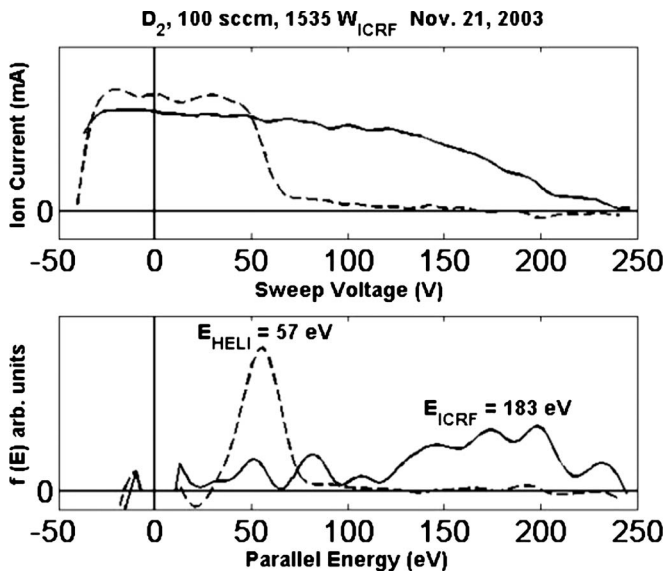


FIG. 14. RPA traces showing the difference between ICH-on and ICH-off. The top panel shows the average of 6 raw sweeps in each curve. The dashed line shows ICH-off and the solid line shows ICH-on. The bottom panel shows the derivative with respect to sweep voltage of the top two curves, which is proportional to energy distribution function. The sweep voltage is referenced to chamber ground instead of plasma potential in these figures. Plasma potential was at ~ 30 V.

the hot component was much hotter than the helicon output was expected to be and the temperature increased with increasing ICH power. The density of the accelerated component was 10%–30% of the hot component, which is a measure of how much charge exchange and scattering degraded the exhaust plume. It is anticipated that the ratio of accelerated to scattered components will improve greatly with improved vacuum pumping capacity. The flow velocity of the cold, fast component increases as the square root of input power, in agreement with the value predicted for an energy absorption rate of 70 eV/ion/kW of transmitted power.

In 2003, an ICH power scan was performed using deuterium propellant at a mass flow rate of 0.140 mg/s, and a fixed helicon power level of 3.5 kW. ICH power was scanned over the range of 254 W to 1535 W, while helicon power remained fixed at 3.5 kW for all shots. The diagnostics used to study the ICH effect on the flowing plasma were the collimated RPA, an rf-compensated Langmuir probe, and a 70 GHz microwave interferometer. Relative to the ICH coupler, the RPA was located 90 cm downstream, the Langmuir probe was 55 cm downstream, and the microwave interferometer was located at 35 cm. At the interferometer location, the magnetic field strength was 20% of its value at the ICH coupler, while the field strength at the RPA was approximately 1% of the value at the coupler.

The upper panel of Fig. 14 shows the current-voltage characteristics with and without ICH power applied, with the energy distributions derived from these characteristics in the lower panel. The dashed curve is the average of six characteristics taken of the helicon-generated plasma without ICH power applied, while the solid curve is the average of six characteristics taken with ICH on.

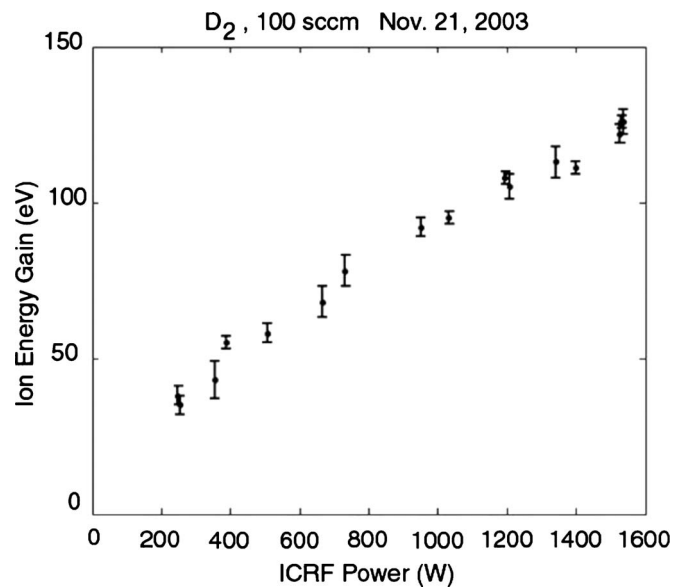


FIG. 15. The energy difference between the location of the peak of the ion energy distribution function for ICH on and the location in the peak for ICH off is plotted as a function of applied ICH power.

The data in Fig. 14 show exactly the expected signature. In contrast to the uncollimated RPA, and as expected, the current was reduced by a factor of about two, while the ion energy showed a second peak with ~ 50 eV more energy than the plasma had prior to turning on the ICH.

Figure 15 shows that the ion energy boost, the difference in the ion energy due to ICH, is directly proportional to the applied ICH. The Langmuir probe indicated that the plasma potential near the RPA was typically increased by ≤ 2 V with the application of ICH power. Assuming that no additional plasma is generated by the ICH power, continuity requires the plasma density to drop as the flow from the helicon (typically ~ 7 –30 eV of kinetic energy, depending on experiment parameters) is abruptly accelerated by the ICH energy boost. This effect is clearly visible in the microwave interferometer data; a typical result is shown in Fig. 16. Again considering continuity, the ratio of the flow velocities with and without ICH should be equal to the reciprocal of the ratio of the plasma densities, with and without ICH. Therefore, we have two independent means of measuring this ratio: the combined RPA and Langmuir probe give the velocity ratio (reciprocal of the density ratio) and the interferometer gives us the density ratio directly. The slight difference in magnetic field strength between the locations of the RPA and interferometer indicate that the flow velocity at the interferometer should be only 10% less than that at the RPA. Details of these measurements are given in Ref. 63. Both the density ratio from the interferometer data and the reciprocal of the velocity ratio are plotted in Fig. 17 for comparison.

B. Increased plasma density

1. 8.3 kW helicon discharge, 1.5 kW ICH

Figure 18 shows the effect of applying 1.3 kW ICH power to deuterium plasma produced by the Boswell coupler operating at 8.3 kW. The gas input rate was 0.140 mg/s. The

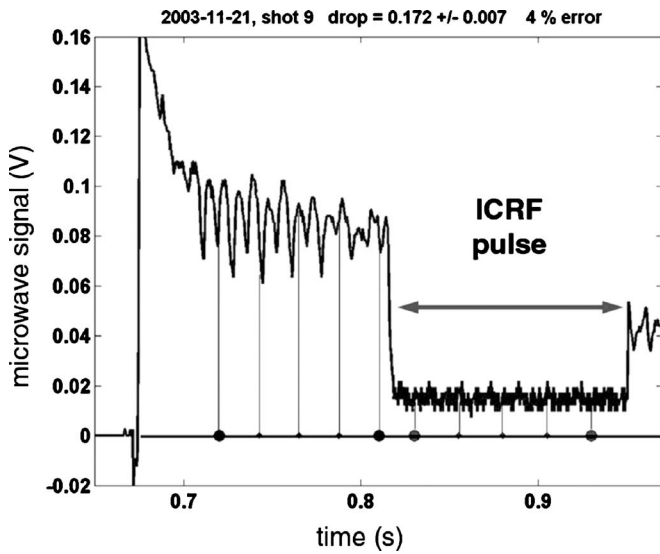


FIG. 16. The raw output of a microwave interferometer is plotted as a function of time during an ICH on shot. The drop in signal corresponds to a drop in density resulting from the combined effect of an acceleration of the plasma and conservation of flux.

figure shows a time series of plasma parameters obtained from least-squares fitting a single drifting Maxwellian to each separate RPA sweep. ICH was turned on at 45.9 s. The data show that the application of ICH doubled the plasma flow velocity. The observed velocity corresponds to an $I_{sp} \sim 9000$ s. The fundamental dynamical quantity is the ion velocity phase space distribution function, F . The distribution functions for both the ICH-on and ICH-off conditions shown in Fig. 18 are plotted in Fig. 19, measured at 0° pitch angle. Figure 19 shows that in the case of deuterium, charge exchange losses between the ICH coupler and the RPA do

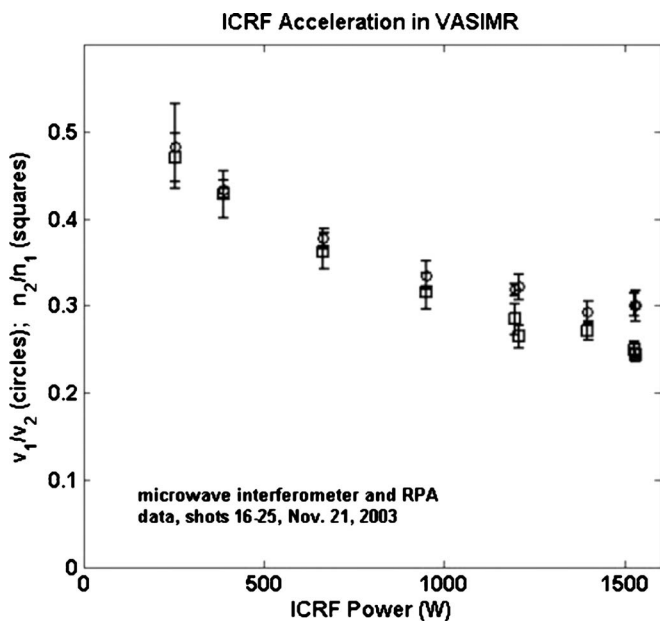


FIG. 17. The ratio of ICH-off to ICH-on plasma velocities (circles) and the ratio of ICH-on to ICH-off plasma densities (squares) are plotted as functions of the applied ICH power.

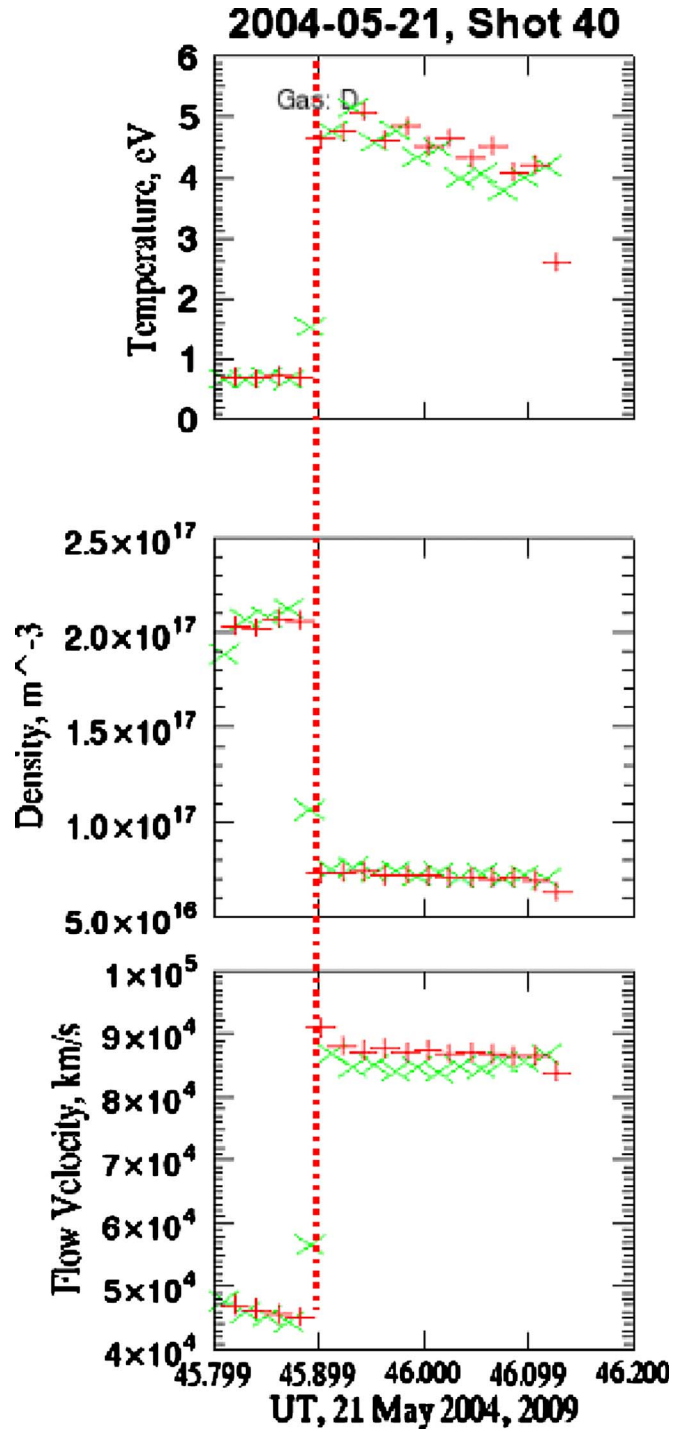


FIG. 18. (Color online) Time series of fit parameters from an ICH-on deuterium plasma shot presented in the same format as Fig. 9. The vertical dashed line show the time when the ICH turned on.

not obscure the effect of ICH, in contrast to the case of helium. In Fig. 19, it is clear that the entire plasma was accelerated.

A bi-Maxwellian model representation was used to the data taken during a scan of the location of the ICH resonance region with respect to the coupler. This scan was performed by increasing the current to the mirror field magnet, which increased the magnetic induction at the mirror thus moving the resonance downstream. Moving the resonance

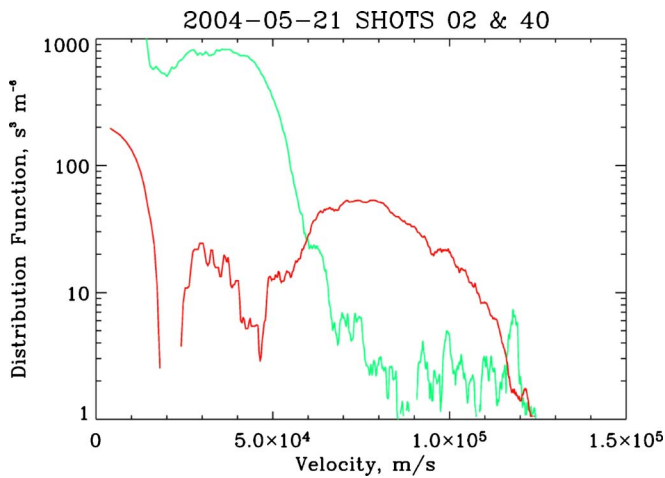


FIG. 19. (Color online) Same as Fig. 6. Distribution function obtained during the ICH-on portion of the deuterium shot shown in Fig. 18 with an ICH-off shot run under otherwise identical conditions. The ICH-off curve is shown as a lighter-colored line.

away from the coupler significantly reduced the plasma loading of the coupler, which means that less rf power was being fed to the plasma. The results of this experiment, interpreted using the bi-Maxwellian approach, are shown in Fig. 20. There are several points to be made concerning the results shown in Fig. 20. The best loading and coupling was achieved when the resonance was located under the coupler. The velocity of the “slow” component was still in excess of 70 km/s near optimum. The density of the faster component exceeds the slow component density, and the estimated output power increase corresponds to or exceeds model estimates for the coupler configuration at that time. These models predicted an ion coupling efficiency of 40%–50% at this plasma density.

The next example of an ICH experiment is a radial scan of the RPA during both ICH ion and off conditions. The results have been interpreted using a single Maxwellian and are shown in Fig. 21. This experiment was performed with a 10 kW helicon discharge. Under these conditions, the plasma loading of the ICH coupler had been increased from ~ 0.2 to $\sim 2 \Omega$, resulting in an increase in coupler efficiency to ~ 0.89 , as shown in Fig. 22.

These results can be integrated to estimate the output power and momentum flux in the exhaust plume. Using the ion flow rate determined by the triple probe, which had a more accurate absolute calibration than the RPA, the power balance corresponds well to model predictions. The measured power input to the ion flux was found to have been

$$P_i = \frac{1}{2} \dot{m}_i (v_{\text{ICH}}^2 - v_{\text{helicon}}^2) = 430 - 591 \text{ W}. \quad (7)$$

Given a coupling efficiency at the time when Figs. 20 and 21 were obtained

$$\eta_B = \frac{P_i}{P_B} = 36\% - 49\%. \quad (8)$$

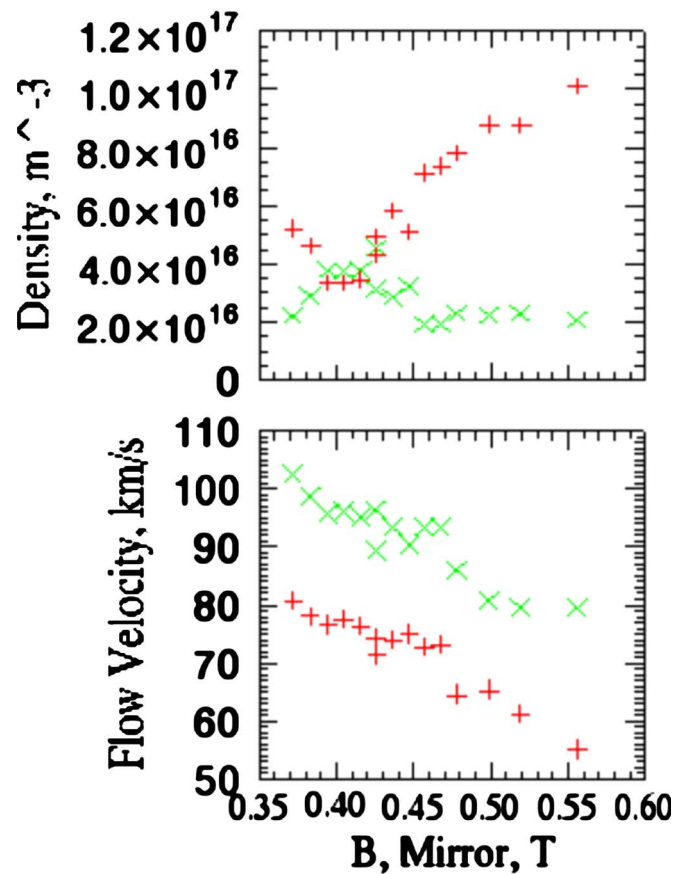
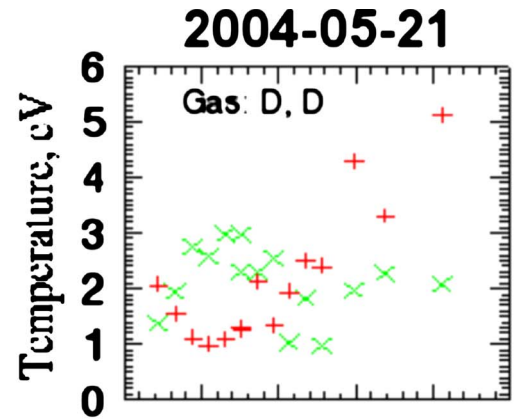


FIG. 20. (Color online) Fit parameters obtained by least-squares fitting drifting bi-Maxwellian representations to the RPA data obtained during a scan of mirror magnet field intensity. From top to bottom, the panels show ion drift velocity, ion density and ion temperature in the frame of the beam. The pluses show the slow, hot component. The X's show the fast, cold accelerated component.

The momentum flux output of the device during these particular runs was estimated to have been $\dot{m}_i v_{\text{ICH}} = 14$ to 19 mN and $\dot{m}_i v_{\text{helicon}} = 7$ to 10 mN. The momentum flux inferred from the RPA and triple probe data agree with the results of a direct momentum flux measurement with a mechanical probe¹⁸ in that the momentum flux with ICH-on is observed to double. The absolute value of the momentum flux inferred

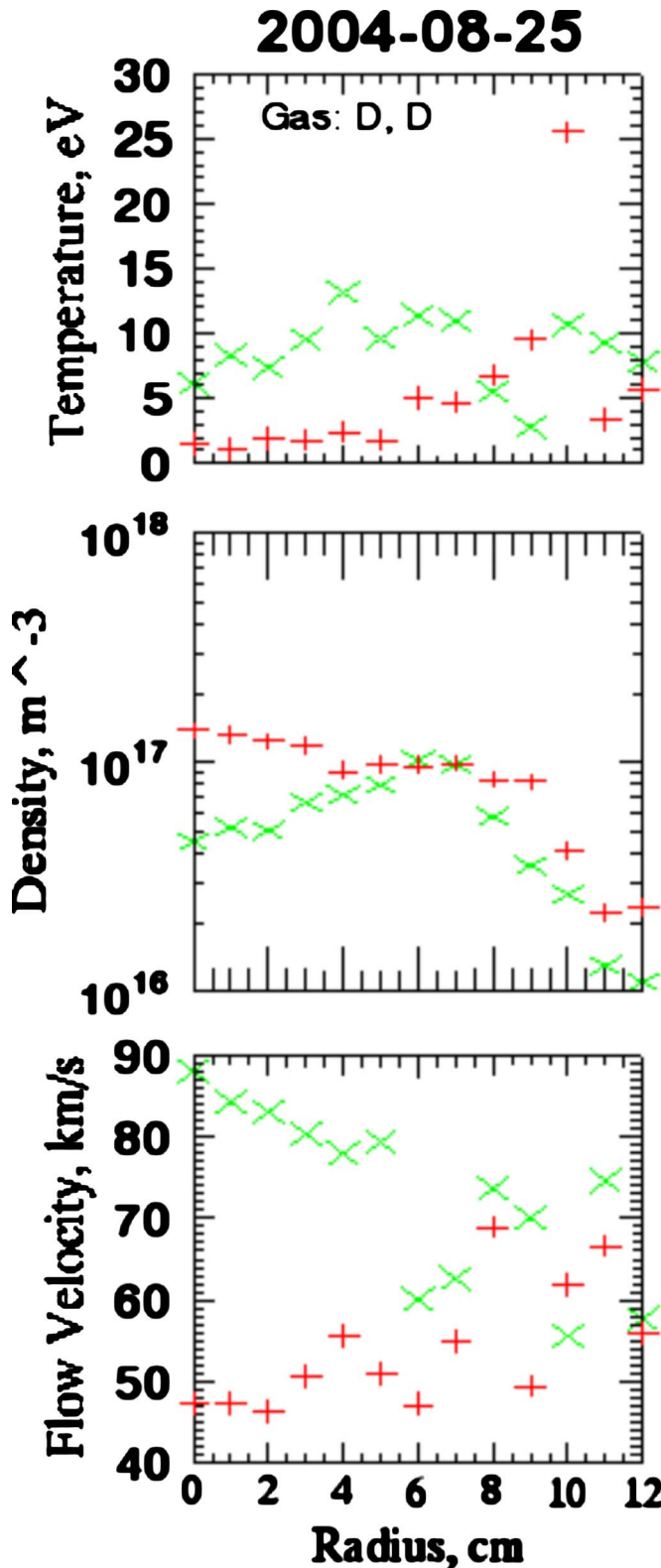


FIG. 21. (Color online) Fit parameters obtained by least-squares fitting drifting Maxwellian representations to RPA data taken while scanning the radial location of the RPA during both ICH-on (X's) and ICH-off (+s) conditions. Each symbol represents the average of all sweeps during a single shot.

from the RPA and probe measurements was not compared directly with the momentum flux probe owing to the fact that the flux probe paddle did not intercept the entire plasma column, and an appropriate model was not yet available.⁸²

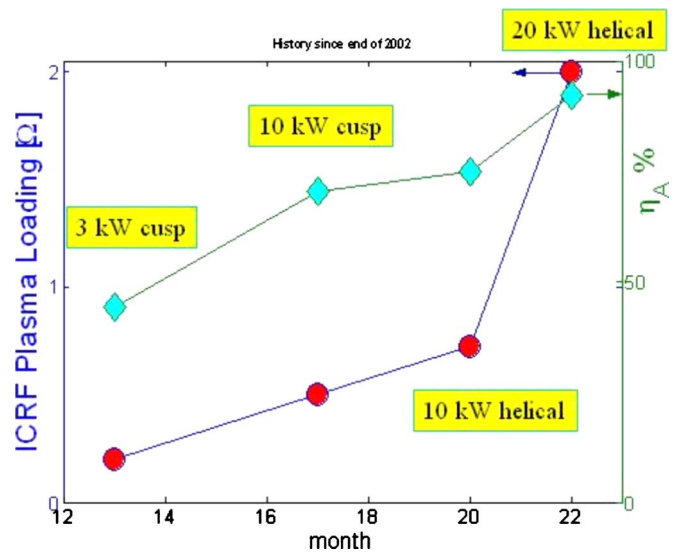


FIG. 22. (Color online) Graph showing time history of the plasma loading of the ICH coupler and corresponding coupler efficiency.

2. 20 kW helicon discharge, 1.5 kW ICH

The 2005 improvements in the helicon discharge increased the available power to 20 kW and reduced the energy cost per ion to ~200 eV per ion pair for deuterium. These improvements combined to give nearly an order of magnitude increase in total ion flux. Conservation of energy considerations required that one expected to observe a substantial reduction in the energy increase per ion obtained with constant power ICH, provided the damping is not so severe as to prevent ICH wave power from penetrating the entire plasma column. Figure 23 compares the ion energy distributions detected by the RPA in a 20 kW deuterium discharge showing the effect of the ICH. The figure shows clear evidence of ion acceleration by 1.5 kW of ICH. The observed energy increase was 17 eV/ion, yielding a plasma with more than twice the bulk kinetic energy obtainable with the helicon alone.

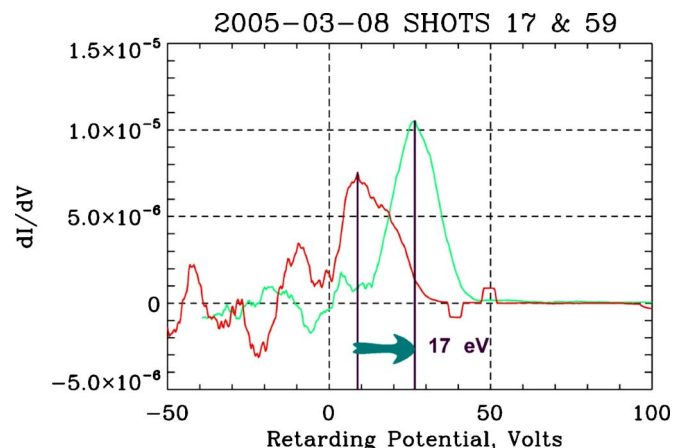


FIG. 23. (Color online) The first derivative of the current-voltage characteristics measured by an RPA with 30° collimation. The lower, darker curve shows a deuterium shot without ICH, and the upper, lighter curve shows a deuterium shot with ICH.

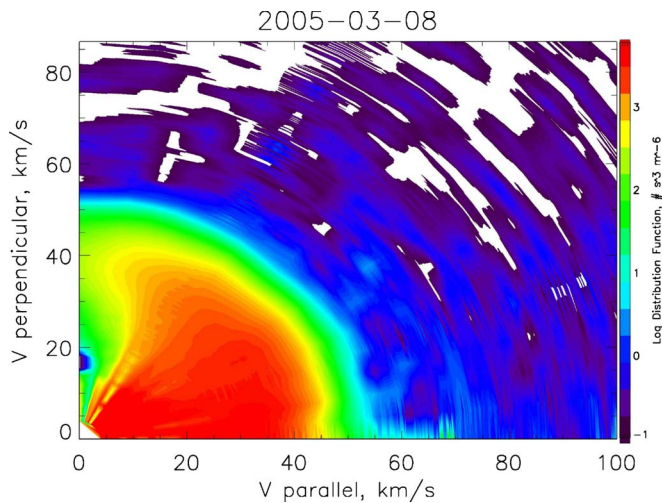


FIG. 24. (Color online) The ion velocity phase space distribution function obtained in a 20 kW deuterium discharge with no ICH. The distribution function grayscale bar scale is logarithmic.

As discussed above, full ion velocity phase space distribution functions can be obtained by rotating the RPA, shot-to-shot. Two-dimensional color contour plots of a planar cut through the distribution function are shown in Fig. 24 for ICH-off and Fig. 25 for ICH-on. A pitch angle of 90° at the location of the maximum field intensity maps to a pitch angle of $\sim 10^\circ$ at the location of the RPA. This result requires that all of the ions in both distributions that have pitch angles $>10^\circ$ must have been scattered, presumably by an ion-neutral collisions. There is a clear, visible difference between the two distributions, indicating that the ICH has accelerated the entire plasma. The reduction in the maximum value of the distribution function in the ICH-on case corresponds to a 0.55 density drop. This decrease is consistent with the results of simultaneous interferometer observations.

The total ion flux during these shots was measured using a number of independent methods, including interferometers, reciprocating triple probe and an array of small planar Lang-

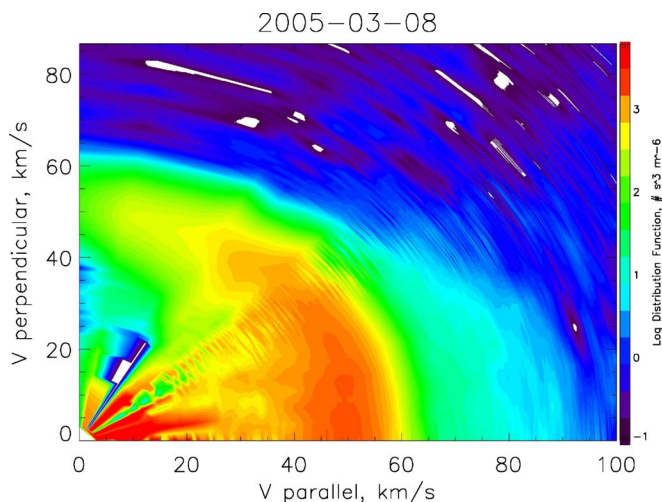


FIG. 25. (Color online) The ion velocity phase space distribution function obtained in a 20 kW deuterium discharge with 1.5 kW of ICH on. The distribution function grayscale bar scale is logarithmic.

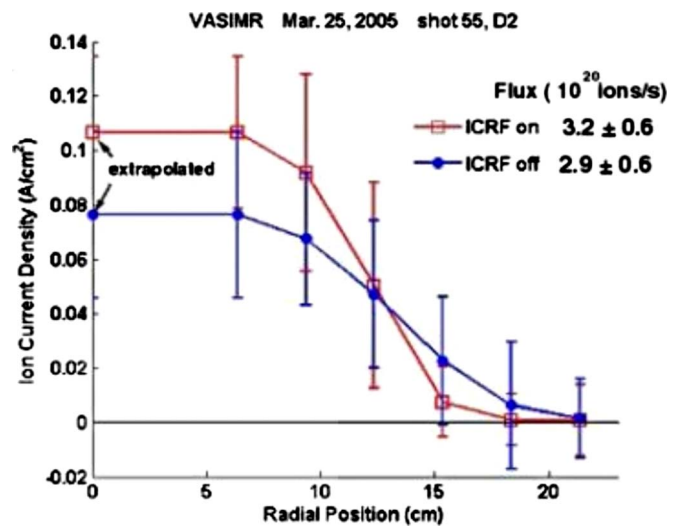


FIG. 26. (Color online) Ion density plotted as a function of radial position during high density discharges similar to those shown in Figs. 23–25. Density was measured by an array of small (~ 1 cm diameter) planar Langmuir probes. Profiles for both ICH-off and ICH-on are compared.

muir probes. The radial density profiles determined by the array of small Langmuir probes for both ICH-on and ICH-off conditions comparable to those shown in Figs. 23–25 are shown in Fig. 26. The plasma flux was measured ~ 0.7 m downstream of the ICH coupler. The figure shows that the profile narrowed when ICH was applied. However, the integrated flux does not change substantially with the application of ICH. A total ion flux was obtained $\Gamma_i = 3.1 \pm 0.6 \times 10^{20}/s$. As noted above, the RPA data indicate that the ICH gave the ions a mean energy increase in $W_{ICH} = 17 \pm 2$ eV. The product of these two numbers gives the total power increase in the exhaust plume, as follows:

$$P_{ion} = \Gamma_i W_{ICH} = 840 \pm 190 \text{ W}. \quad (9)$$

The ICH power that has been radiated into the plasma may be estimated using the ICH coupler efficiency, $\eta_A = 89\%$, which was determined from the plasma loading measurements

$$P_{plasma} = \eta_A P_{ICH} = 1.25 \text{ kW}. \quad (10)$$

Finally, we obtain an estimate of the efficiency of the ICH process, as follows:

$$\eta_{ICH} = \frac{P_{ion}}{P_{plasma}} = 67\% \pm 15\%. \quad (11)$$

Absorption efficiency of this order is high enough to suggest the possibility that the ICW was fully damped prior to reaching the center of the plasma column. This situation was investigated by means of another RPA radial scan (Fig. 27). Figure 27 indeed shows a drop in bulk flow velocity and a corresponding increase in ion density in the innermost 1 cm of the plasma column. This apparent hole is based on a single point observation in this radial scan and may correspond to an asymmetry or a shot to shot variation. This hole would indicate that 1.3 kW is insufficient signal strength to fully illuminate the discharge that the experiment was producing. The corresponding perpendicular absorption scale length in

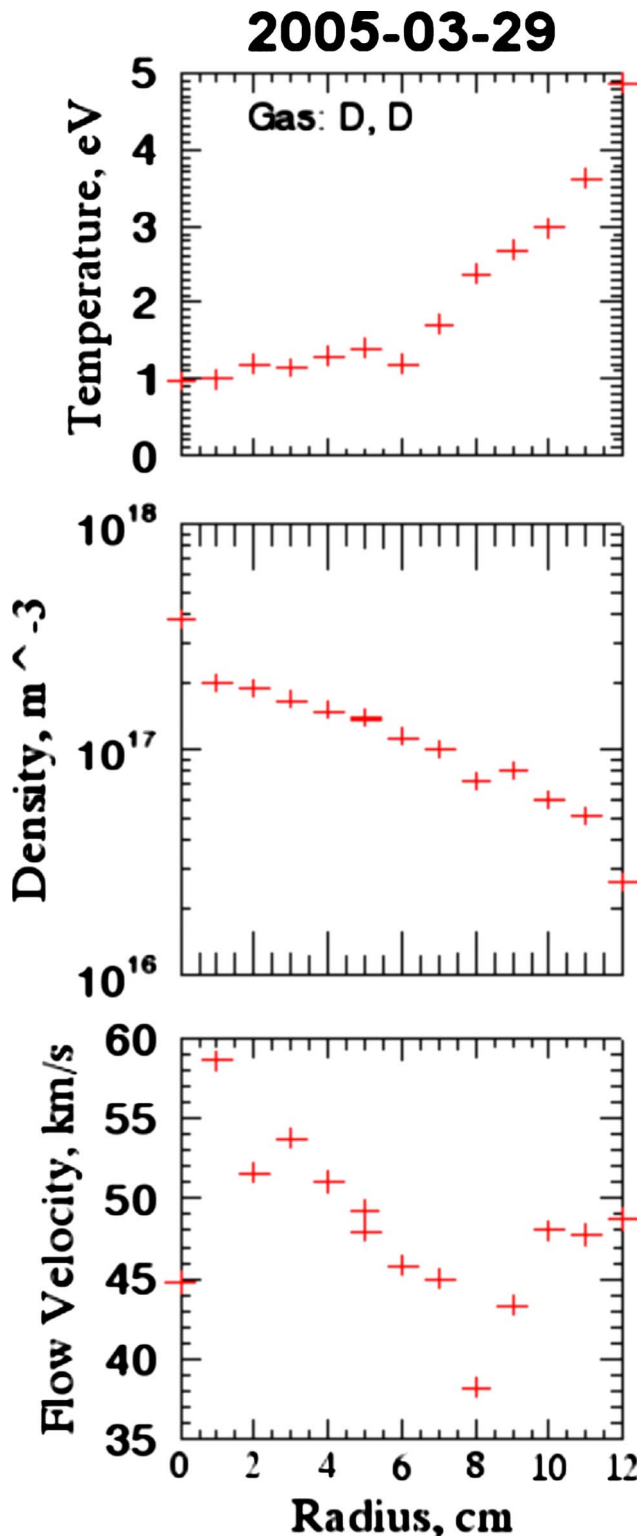


FIG. 27. (Color online) Fit parameters obtained by least-squares fitting drifting Maxwellian representations to RPA data taken while scanning the radial location of the RPA during ICH-on (X's) conditions during high density discharges similar to those shown in Figs. 23–25. Each symbol represents the average of all sweeps during a single shot.

the resonance region was determined to have been 0.7 cm by mapping Fig. 27 back to the resonance region. The implications of this number will be discussed below. Since the data in Figs. 23 and 25 were taken at the center of the column, it

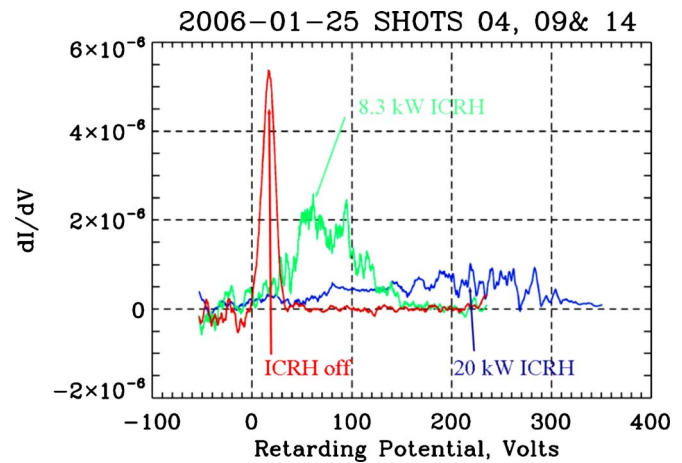


FIG. 28. (Color online) Comparison of ion energy distributions for 0, 8.3, and 20 kW of ICH power in deuterium plasma, input flow rate 0.625 mg/s, and 20 kW helicon power.

is likely that the ion energization, power deposited and ICH efficiency estimates just presented were systematically low.

At this point in the series of experiments, it had been demonstrated that high efficiency single-pass ion cyclotron coupling and subsequent conversion to axial momentum had been achieved in a trans-sonic deuterium plasma.

C. Increased plasma density, 20 kW ICH

The final step in the progressive improvement process that will be described in this paper was an order of magnitude increase in the available ICH power, up to 20 kW. The effect of this increase in ICH power level was dramatic and clear. Figure 28 shows the derivative with respect to voltage of the current-voltage RPA data from three shots with different ICH power levels, 0, 8.3, and 20 kW. The derivative is proportional to the ion energy distribution and shows that 20 kW of ICH added approximately 200 eV to the mean energy of the deuterium ions in this configuration. The ion velocity phase space distribution functions corresponding to Fig. 28 are shown in Fig. 29. The ICH off distribution is an elegant example of a cold, Maxwellian ion distribution. The

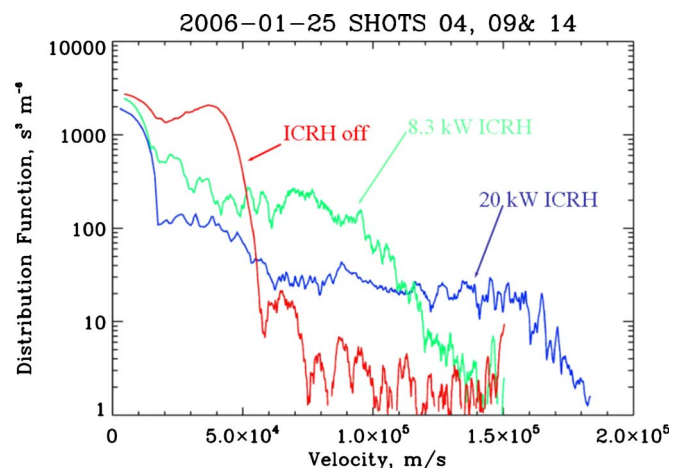


FIG. 29. (Color online) Comparison of ion velocity distributions for the same three shots as in Fig. 28.

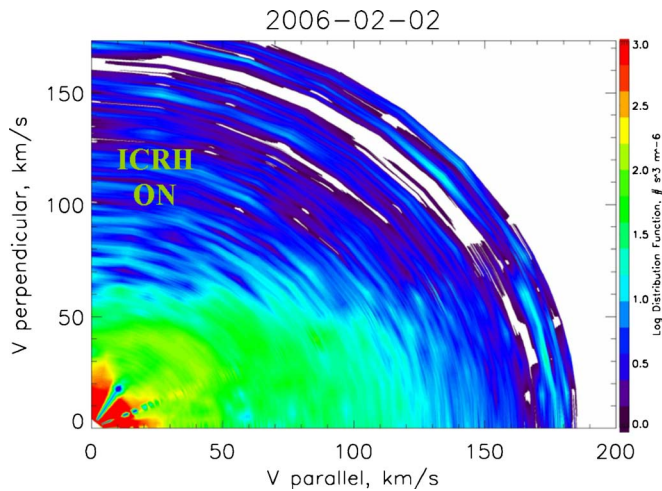


FIG. 30. (Color online) Ion velocity phase space distribution function, 14 kW ICH on, in deuterium plasma, input flow rate 0.625 mg/s, and 20 kW helicon power.

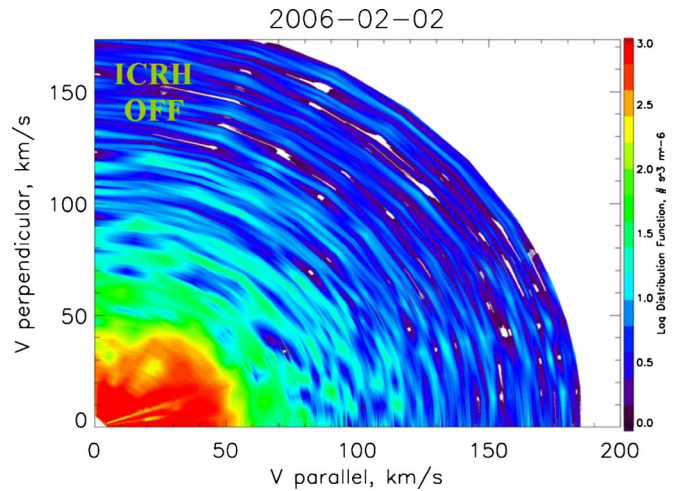


FIG. 31. (Color online) Ion velocity phase space distribution function, ICH off in deuterium plasma, input flow rate 0.625 mg/s, and 20 kW helicon power.

two ICH-on distributions show that the plasma was drifting faster and was hotter in the rest frame of the beam. This result is somewhat in contrast to the 1.5 kW results, where the beam remained cold in the beam rest frame. The 20 kW curve in particular shows the presence of multiple Maxwellians with different drift speeds and temperatures. We take this lower energy “filled in” character of the distribution function to be a signature of charge exchange with background neutrals. This charge exchange is a consequence of inadequate vacuum pump capacity and high background neutral density. It should also be noted that the RPA voltage sweep was not operated to high enough voltage (360 V) to stop the ion current completely. The highest energy tail of the ion distribution extended to >350 eV energy.

The pitch angle distribution of the accelerated ions was investigated using the same method previously used to produce Fig. 25. The ICH power was limited to 14 kW so that the available sweep voltage stopped the entire population. The two-dimensional ion velocity phase space distributions measured with 14 kW of ICH and no ICH are shown in Figs. 30 and 31. The presence of a high velocity, somewhat conical jet of plasma is clearly evident in Fig. 30. As above, 90° pitch angle at the location of the ICH coupler maps to 10° pitch angle at the location of the RPA, which means that all the high velocity ions observed at greater pitch angles in Fig. 30 are indicative of both the somewhat coarse collimation of the RPA and the presence of ion-neutral scattering.

Typically, reduced RPA data figures from this experiment present all three of the fitted parameters, plotted either as functions of time within a single shot (e.g., Fig. 18), or as functions of other parameters varied on a shot-to-shot basis. Figure 32 shows another example of a time series plot, showing the effect of a 100 ms burst of 14 kW of ICH power on deuterium plasma. From top to bottom, the figure shows ion temperature in the frame of the beam, ion density, and ion drift speed. During the ICH burst, the ion temperature increased from 1 to 35 eV, the density dropped by a factor of 3 and the drift speed increased by a factor of 4. The apparent increase in total flux seems to indicate that the ICH was

acting to increase the ionization of the gas, which indicates that the helicon was not optimized for this shot. The temperature shown was effectively the parallel temperature of the ions in the frame moving with the beam. The parallel ion temperature increase was much larger than the increases seen in previous work.²⁷ The apparent waste of energy in adding to the parallel heat content of the beam is not as severe as it might seem at first glance. At least two processes were responsible. First, there was a relatively large amount of ion neutral scattering owing to the pumping problem alluded to above. Second, the ICH process has a dispersive component that depends on the incident gyrophase of the ions relative to the ICH waveform. The amount of energy that an ion obtains in the resonance region depends, in part, on this phase angle. This energy spread appears to the least-squares fit as an apparent parallel temperature. However, it does not represent waste heat content of the beam. Finally, at high input power, nonlinear broadening of the resonance,⁸³ and changes of the phase of the ion orbits will act to increase the parallel heating rate of the ions. From a practical standpoint, the smearing out of the resonance, combined with the Doppler shift, will allow a larger fraction of the ions to absorb energy from the wave field,⁵¹ which is a very desirable outcome.

Figure 33 shows the results from scanning the RPA in radius with 14 kW of ICH power applied. The data indicate that the plasma column had a roughly constant temperature and density out to a radius of 9 cm. The velocity curve shows a generally parabolic profile with a dip in the center. The dip in the center is similar to the dip in the center of Fig. 27 and may indicate that the ICH signal was fully absorbed prior to penetrating all the way to the center of the plasma. However, this apparent hole is based on a single point observation in this radial scan and may correspond to an asymmetry or a shot to shot variation. The corresponding perpendicular absorption scale length in the resonance region was determined to have been 1.0 cm by mapping Fig. 33 back to the resonance region. It is rather challenging to determine if the observed absorption distance corresponds to theory or not. The situation was too complicated and structured to allow us to

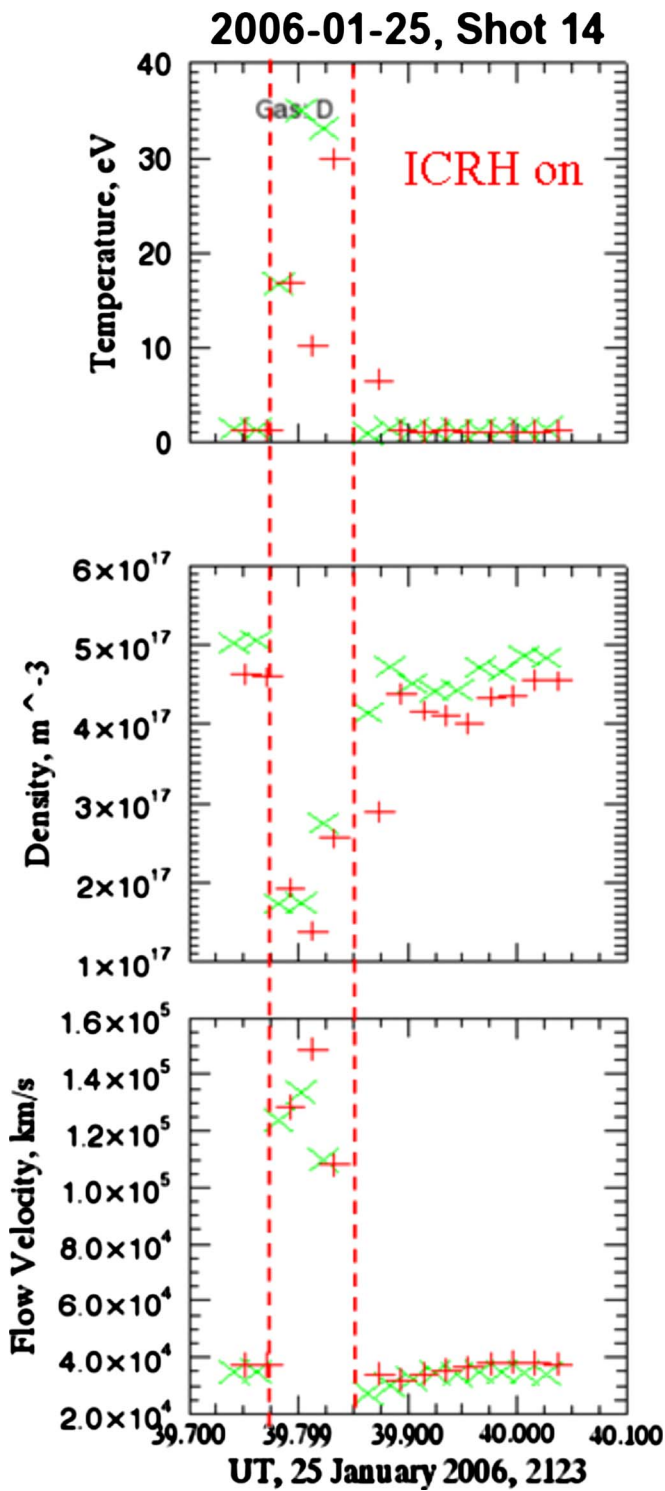


FIG. 32. (Color online) Time series of fit parameters obtained by least-squares fitting a drifting Maxwellian representation to the raw RPA data during ICH deuterium plasma shots. From bottom to top, the panels show ion drift velocity, ion density, and ion temperature in the frame of the beam.

apply the WKB approximation with any confidence. Since the density and therefore the index of refraction scale length was comparable to the nominal perpendicular “wavelength,” the concept of a perpendicular “wave number” was not well defined. Since the idea of a central dip is based on just two shots in two radial scans, its existence is quite uncertain. Finally, detailed ion and electron distribution function mea-

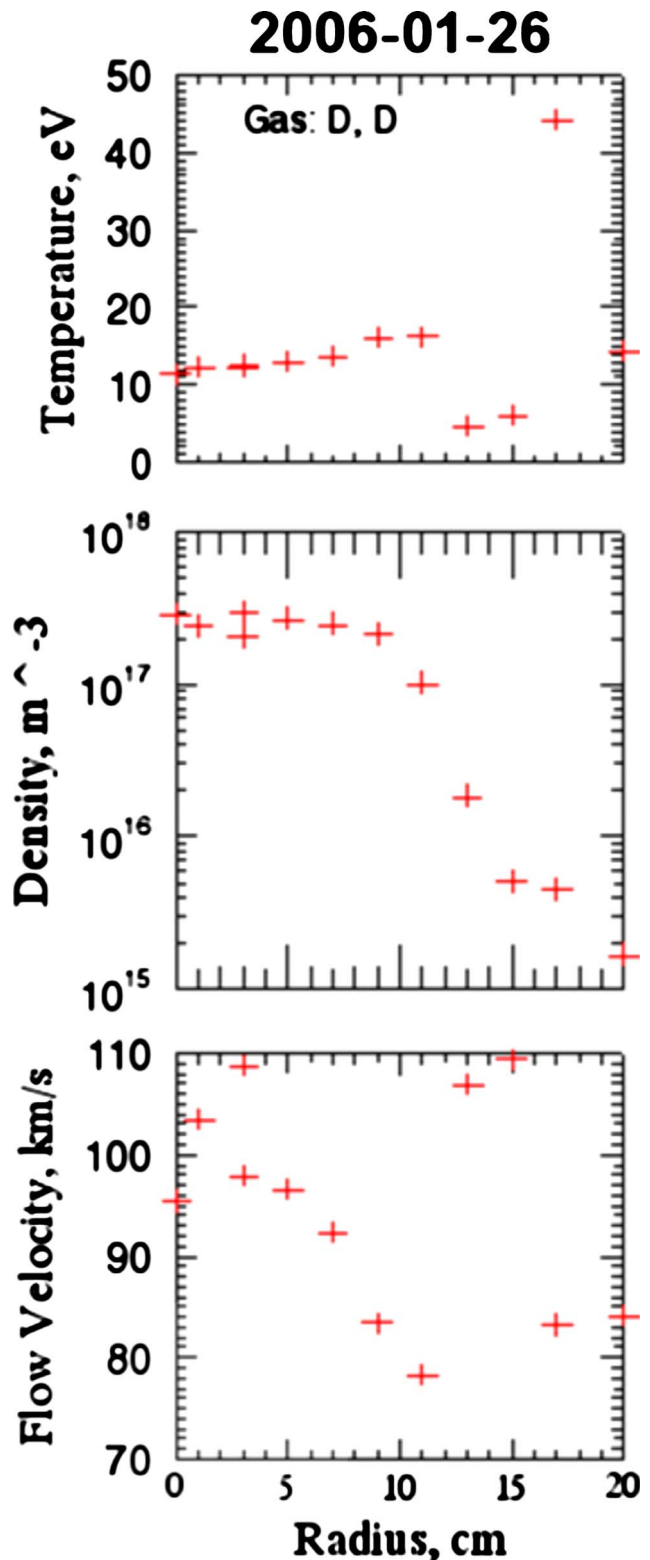


FIG. 33. (Color online) A radial scan of the RPA, showing fit parameters obtained by least-squares fitting a drifting Maxwellian representation to the raw RPA data during ICH deuterium plasma shots as functions of radius from the center of the beam. From bottom to top, the panels show ion drift velocity, ion density, and ion temperature in the frame of the beam.

surements were not made within the resonance region. Since the apparatus no longer exists, no more data can be obtained.

Figure 34 shows the comparison of two scans of ICH power for two different gas inlet flow rates, 0.625 mg/s,

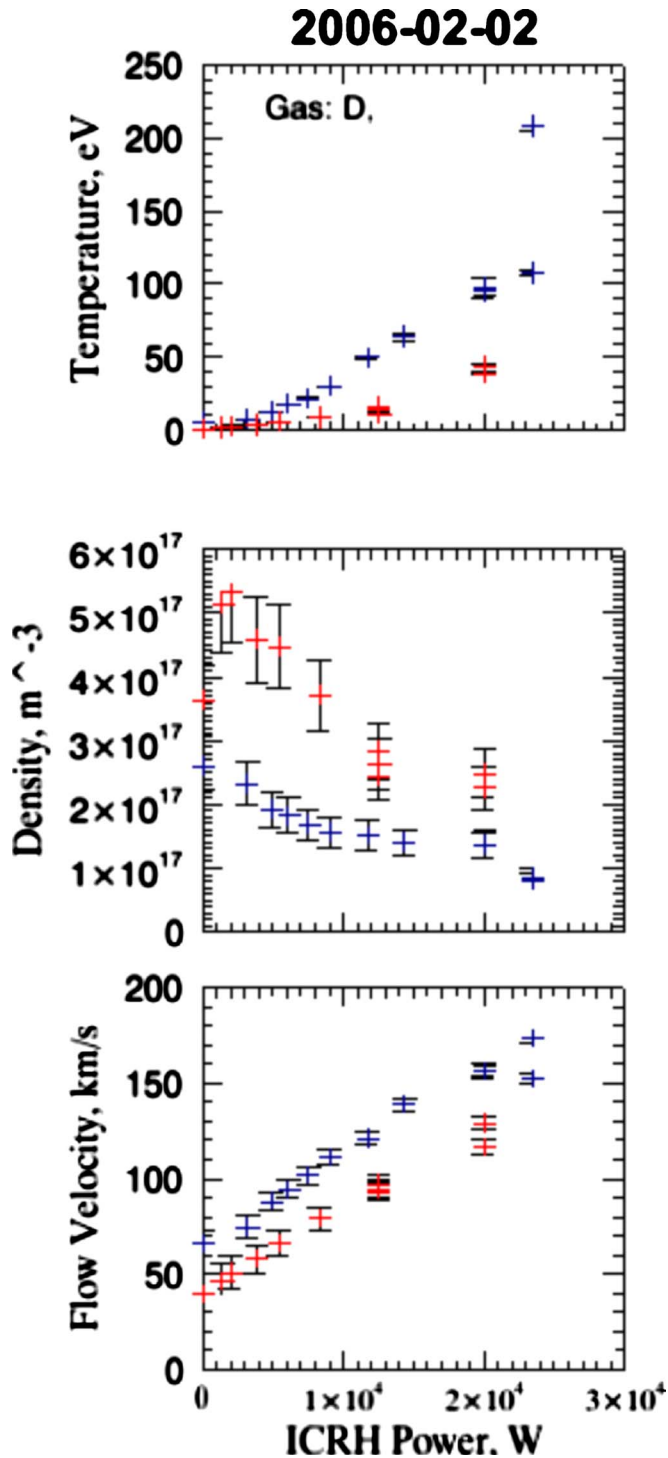


FIG. 34. (Color online) Scans of ICH power for two different flow rates and helicon power levels, showing fit parameters obtained by least-squares fitting a drifting Maxwellian representation to the raw RPA data during ICH deuterium plasma shots as functions of ICH power. From bottom to top, the panels show ion drift velocity, ion density and ion temperature in the frame of the beam. The meaning of the two separate curves is discussed in the text.

which is plotted in red and appears as the top curve in the middle panel and the bottom curve in the other two, and 0.35 mg/s, which is plotted in blue and is the other curve in each panel. The helicon power was reduced to 17 kW in the lower flow rate shot series. The purpose of this set of experiments was to demonstrate explicitly the variable specific im-

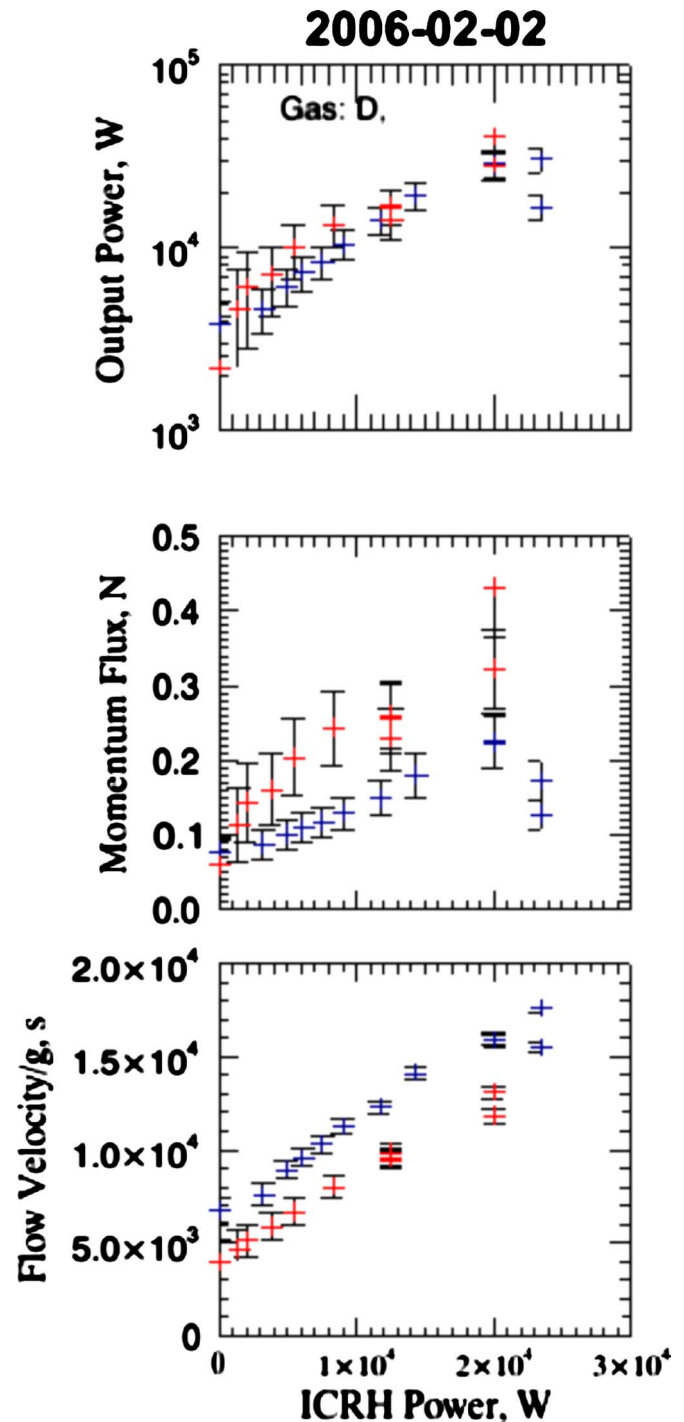


FIG. 35. (Color online) Scans of ICH power for two different flow rates and helicon power levels, showing parameters inferred from the fit parameters shown in the previous figure as functions of ICH power. From bottom to top, the panels show output power, thrust and specific impulse. The meaning of the two separate curves is discussed in the text.

pulse capability of the VASIMR. The lower flow rate shots produced an output that was 20% faster, had a much higher parallel temperature, and were lower in density than the high flow shots. These data can be used to estimate the thrust and output power, by integrating across the plume profile shown in Fig. 33 for each of the shots shown in Fig. 34. The results are shown in Fig. 35. The output power is virtually the same in each case, whereas the lower flow produces lower thrust

and higher specific impulse, which is as expected, and which verifies the fundamental constant power throttling premise of the VASIMR[®] concept.

IV. CONCLUSIONS

Substantial progress was made in the development of the VASIMR[®] engine by the VX-50 proof of concept experiments. The operating power level of the helicon discharge was increased by nearly an order of magnitude, from 2 to 20–24 kW. The energy cost per ion pair was reduced to ~200–250 eV. The understanding of helicon physics obtained with the VX-50 has enabled the team to reduce the ionization cost by another factor of 3 in the current VX-200 device. Plasma loading of the ICH coupler increased with increasing total ion flux and plasma density. Using the VX-50 maximum helicon discharge output, loading impedance in excess of 2 Ω was obtained, which corresponds to $\eta_A > 90\%$. Single-pass ICH has been demonstrated repeatedly in a variety of configurations. High power (20 kW) ICH has been achieved. $\eta_B > 80\%$ has been obtained with deuterium. Increases in the parallel ion temperature observed at high ICH power may be evidence for nonlinear broadening of the absorption resonance. No macroscopic power limiting beam instabilities were observed. Auroral process simulation experiments are now possible in the VASIMR.

ACKNOWLEDGMENTS

NASA Johnson Space Center (Grant No. NAG 9-1524) and the Texas Higher Education Coordinating Board Advanced Technology Program (Project No. 003652-0464-1999) sponsored this research.

- ¹K. Sankaran, L. Cassady, A. D. Kodys, and E. Y. Choueiri, in *Astrodynamics, Space Missions, and Chaos*. Annals of the New York Academy of Sciences Vol. 1017, edited by E. Belbruno, D. Folta, and P. Gurfil (New York Academy of Sciences, New York, NY, 2004), pp. 450–467.
- ²F. R. Chang Díaz, *53rd International Astronautical Congress/The World Space Congress*, 10–19 October 2002 (American Institute of Aeronautics and Astronautics, Houston, Texas, 2002).
- ³E. A. Bering III, F. R. Chang Díaz, and J. P. Squire, *Radio Sci. Bull.* **310**, 92 (2004).
- ⁴F. R. Chang Díaz and J. L. Fisher, *Nucl. Fusion* **22**, 1003 (1982).
- ⁵F. R. Chang Díaz, *Bull. Am. Phys. Soc.* **DPP97**, pThp.M2.01 (1997).
- ⁶F. R. Chang Díaz, *Open Systems*, Novosibirsk, Russia, 27–31 July 1998 [Trans. Fusion Technol. **35**, 87 (1999)].
- ⁷F. R. Chang Díaz, J. P. Squire, A. V. Ilin, G. E. McCaskill, T. X. Nguyen, D. S. Winter, A. J. Petro, G. W. Goebel, L. D. Cassady, K. A. Stokke, C. E. Dexter, T. P. Graves, L. Amador, Jr., M. D. Carter, F. W. Baity, Jr., G. C. Barber, R. H. Goulding, and D. C. Sparks, *International Conference of Electromagnetics in Advanced Applications ICEAA '99*, 13–17 September 1999 (Lifografia Geda, Torino, Italy, 1999), pp. 99–102.
- ⁸F. R. Chang Díaz, J. P. Squire, E. A. Bering III, J. A. George, A. V. Ilin, A. J. Petro, and L. Cassady, *39th American Institute of Aeronautics and Astronautics Aerospace Sciences Meeting and Exhibit*, 8–11 January 2001 (American Institute of Aeronautics and Astronautics, Reno, NV, 2001).
- ⁹F. R. Chang Díaz, J. P. Squire, T. Glover, A. J. Petro, E. A. Bering III, F. W. J. Baity, R. H. Goulding, M. D. Carter, R. D. Bengtson, and B. N. Breizman, *42nd American Institute of Aeronautics and Astronautics Aerospace Sciences Meeting and Exhibit*, 5–8 January 2004 (American Institute of Aeronautics and Astronautics, Reno, NV, 2004).
- ¹⁰E. A. Bering III, F. R. Chang Díaz, J. P. Squire, T. W. Glover, R. D. Bengtson, and M. Brukardt, *42nd American Institute of Aeronautics and Astronautics Aerospace Sciences Meeting and Exhibit*, 5–8 January 2004 (American Institute of Aeronautics and Astronautics, Reno, NV, 2004).
- ¹¹N. J. Fisch, *Phys. Rev. Lett.* **41**, 873 (1978).

- ¹²S. N. Golovato, K. Brau, J. Casey, J. Coleman, M. J. Gerver, W. Guss, G. Hallock, S. Horne, J. Irby, R. Kumazawa, J. Kesner, B. Lane, J. Machuzak, T. Moran, R. Myer, R. S. Post, E. Sevillano, D. K. Smith, J. D. Sullivan, R. Torti, L. Wang, Y. Yasaka, X. Z. Yao, and J. Zielinski, *Phys. Fluids* **31**, 3744 (1988).
- ¹³Y. Yasaka, R. Majeski, J. Browning, N. Hershkowitz, and D. Roberts, *Nucl. Fusion* **28**, 1765 (1988).
- ¹⁴D. Swanson, *Plasma Waves* (Academic, New York, 1989).
- ¹⁵T. H. Stix, *Waves in Plasma* (American Institute of Physics, New York, 1992).
- ¹⁶E. A. Bering III, M. Brukardt, F. R. Chang Díaz, J. P. Squire, V. T. Jacobson, R. D. Bengtson, J. N. Gibson, and T. W. Glover, *40th American Institute of Aeronautics and Astronautics Aerospace Sciences Meeting and Exhibit*, 14–17 January 2002 (American Institute of Aeronautics and Astronautics, Reno, NV, 2002).
- ¹⁷E. A. Bering III, M. S. Brukardt, W. A. Rodriguez, F. R. Chang Díaz, J. P. Squire, V. T. Jacobson, A. V. Ilin, D. S. Winter, R. D. Bengtson, J. N. Gibson, T. W. Glover, and D. G. Chambers, *53rd International Astronautical Congress/The World Space Congress*, 10–19 October 2002 (American Institute of Aeronautics and Astronautics, Houston, Texas, 2002).
- ¹⁸D. G. Chavers and F. R. Chang Díaz, *Rev. Sci. Instrum.* **73**, 3500 (2002).
- ¹⁹B. N. Breizman and A. V. Arefiev, *Phys. Plasmas* **8**, 907 (2001).
- ²⁰E. G. Shelley, R. D. Sharp, and R. G. Johnson, *Geophys. Res. Lett.* **3**, 654, doi:10.1029/GL003i011p00654 (1976).
- ²¹R. D. Sharp, R. G. Johnson, and E. G. Shelley, *J. Geophys. Res.* **82**, 3324, doi:10.1029/JA082i022p03324 (1977).
- ²²F. S. Mozer, C. W. Carlson, M. K. Hudson, R. B. Torbert, B. Parady, J. Yatteau, and M. C. Kelley, *Phys. Rev. Lett.* **38**, 292 (1977).
- ²³A. G. Ghielmetti, R. G. Johnson, R. D. Sharp, and E. G. Shelley, *Geophys. Res. Lett.* **5**, 59, doi:10.1029/GL005i001p00059 (1978).
- ²⁴E. G. Shelley, *Space Sci. Rev.* **23**, 465 (1979).
- ²⁵R. D. Sharp, R. G. Johnson, and E. G. Shelley, *J. Geophys. Res.* **84**, 480, doi:10.1029/JA084iA02p00480 (1979).
- ²⁶H. L. Collin, R. D. Sharp, E. G. Shelley, and R. G. Johnson, *J. Geophys. Res.* **86**, 6820, doi:10.1029/JA086iA08p06820 (1981).
- ²⁷M. Zintl, R. McWilliams, and N. Wolf, *Phys. Plasmas* **2**, 4432 (1995).
- ²⁸M. André, P. Norqvist, L. Andersson, L. Eliasson, A. L. Eriksson, L. Blomberg, R. Erlandson, and J. Waldemark, *J. Geophys. Res.* **103**, 4199, doi:10.1029/97JA00855 (1998).
- ²⁹J. M. Kindel and C. F. Kennel, *J. Geophys. Res.* **76**, 3055, doi:10.1029/JA076i013p03055 (1971).
- ³⁰E. Ungstrup, D. M. Klumppar, and W. J. Heikilla, *J. Geophys. Res.* **84**, 4289, doi:10.1029/JA084iA08p04289 (1979).
- ³¹M. Ashour-Abdalla, H. Okuda, and C. Z. Cheng, *Geophys. Res. Lett.* **8**, 795, doi:10.1029/GL008i007p00795 (1981).
- ³²T. Chang, G. B. Crew, N. Hershkowitz, J. R. Jasperse, J. M. Retterer, and J. D. Winningham, *Geophys. Res. Lett.* **13**, 636, doi:10.1029/GL013i007p00636 (1986).
- ³³R. E. Erlandson, L. J. Zanetti, T. A. Potemra, M. Andre, and L. Matson, *Geophys. Res. Lett.* **15**, 421, doi:10.1029/GL015i005p00421 (1988).
- ³⁴R. Erlandson, L. Zanetti, M. Acuna, A. Eriksson, L. Eliasson, M. Boehm, and L. Blomberg, *Geophys. Res. Lett.* **21**, 1855, doi:10.1029/94GL01363 (1994).
- ³⁵J. Borovsky, *J. Geophys. Res.* **89**, 2251, doi:10.1029/JA089iA04p02251 (1984).
- ³⁶R. McWilliams and R. Koslover, *Phys. Rev. Lett.* **58**, 37 (1987).
- ³⁷E. A. Bering III, M. C. Kelley, and F. S. Mozer, *J. Geophys. Res.* **80**, 4612, doi:10.1029/JA080i034p04612 (1975).
- ³⁸E. A. Bering and F. S. Mozer, *J. Geophys. Res.* **80**, 3961, doi:10.1029/JA080i028p03961 (1975).
- ³⁹M. C. Kelley, E. A. Bering III, and F. S. Mozer, *Phys. Fluids* **18**, 1590 (1975).
- ⁴⁰P. M. Kintner, M. C. Kelley, and F. S. Mozer, *Geophys. Res. Lett.* **5**, 139, doi:10.1029/GL005i002p00139 (1978).
- ⁴¹P. M. Kintner, M. C. Kelley, R. D. Sharp, A. G. Ghielmetti, M. Temerin, C. Cattell, P. F. Mizera, and J. F. Fennell, *J. Geophys. Res.* **84**, 7201, doi:10.1029/JA084iA12p07201 (1979).
- ⁴²P. M. Kintner, *Geophys. Res. Lett.* **7**, 585, doi:10.1029/GL007i008p00585 (1980).
- ⁴³P. M. Kintner, W. Scales, J. Vago, A. Yau, B. Whalen, R. Arnoldy, and T. Moore, *J. Geophys. Res.* **96**, 9627, doi:10.1029/91JA00563 (1991).
- ⁴⁴E. A. Bering III, *Geophys. Res. Lett.* **10**, 647, doi:10.1029/GL010i008p00647 (1983).
- ⁴⁵E. A. Bering III, *J. Geophys. Res.* **89**, 1635, doi:10.1029/

- JA089iA03p01635 (1984).
- ⁴⁶J. Bonnell, P. Kintner, J. Wahlund, K. Lynch, and R. Arnoldy, *Geophys. Res. Lett.* **23**, 3297, doi:10.1029/96GL03238 (1996).
- ⁴⁷P. M. Kintner, J. Bonnell, R. Arnoldy, K. Lynch, C. Pollock, and T. Moore, *Geophys. Res. Lett.* **23**, 1873, doi:10.1029/96GL01863 (1996).
- ⁴⁸P. M. Kintner, P. W. Schuck, and J. R. Franz, *Phys. Plasmas* **7**, 2135 (2000).
- ⁴⁹P. M. Kintner, J. Franz, P. Schuck, and E. Klatt, *J. Geophys. Res.* **105**, 21237, doi:10.1029/1999JA000323 (2000).
- ⁵⁰W. E. Amatucci, D. N. Walker, G. Ganguli, D. Duncan, J. A. Antoniadis, J. H. Bowles, V. Gavriushchaka, and M. E. Koepke, *J. Geophys. Res.* **103**, 11711, doi:10.1029/98JA00659 (1998).
- ⁵¹D. Correll, H. Boehmer, N. Rynn, and R. Stern, *Phys. Fluids* **20**, 822 (1977).
- ⁵²S. Cartier, N. D'Angelo, and R. Merlino, *J. Geophys. Res.* **91**, 8025, doi:10.1029/JA091iA07p08025 (1986).
- ⁵³A. Fruchtman, *Bull. Am. Phys. Soc.* **50**, 109 (2005).
- ⁵⁴A. Fruchtman, *Phys. Rev. Lett.* **96**, 065002 (2006).
- ⁵⁵J. P. Squire, F. R. Chang Díaz, V. T. Jacobson, G. E. McCaskill, R. D. Bengtson, and R. H. Goulding, *36th American Institute of Aeronautics and Astronautics/ASME/SAE/ASEE Joint Propulsion Conference*, 17–19 July 2000 (American Institute of Aeronautics and Astronautics, Huntsville, Alabama, 2000).
- ⁵⁶A. Petro, F. R. Chang Díaz, A. V. Ilin, and J. P. Squire, *40th American Institute of Aeronautics and Astronautics Aerospace Sciences Meeting and Exhibit*, 14–17 January 2002 (American Institute of Aeronautics and Astronautics, Reno, NV, 2002).
- ⁵⁷F. R. Chang Díaz, *AIP Conf. Proc.* **595**, 3 (2001).
- ⁵⁸R. W. Boswell, *Plasma Phys. Controlled Fusion* **26**, 1147 (1984).
- ⁵⁹F. F. Chen, *Plasma Phys. Controlled Fusion* **33**, 339 (1991).
- ⁶⁰R. W. Boswell and F. F. Chen, *IEEE Trans. Plasma Sci.* **25**, 1229 (1997).
- ⁶¹R. W. Boswell and C. Charles, *28th International Electric Propulsion Conference, IEPC 2003*, 17–21 March 2003 (Electric Rocket Propulsion Society, Toulouse, France, 2003), p. 332.
- ⁶²A. V. Arefiev and B. N. Breizman, *Phys. Plasmas* **12**, 043504 (2005).
- ⁶³T. W. Glover, F. R. Chang Díaz, V. T. Jacobson, A. G. Tarditi, J. P. Squire, D. G. Chavers, and M. D. Carter, *40th American Institute of Aeronautics and Astronautics/ASME/SAE/ASEE Joint Propulsion Conference and Exhibit*, 12–14 July 2004 (American Institute of Aeronautics and Astronautics, Fort Lauderdale, FL, 2004).
- ⁶⁴E. A. Bering III, J. P. Squire, G. McCaskill, V. Jacobson, T. W. Glover, and M. Brukardt, *43rd American Institute of Aeronautics and Astronautics Aerospace Sciences Meeting and Exhibit*, 10–13 January 2005 (American Institute of Aeronautics and Astronautics, Reno, NV, 2005).
- ⁶⁵F. R. Chang Díaz, J. P. Squire, A. V. Ilin, A. J. Petro, V. Jacobson, G. McCaskill, A. G. Tarditi, D. A. Winter, R. D. Bengtson, B. N. Breizman, F. W. Baity, Jr., M. D. Carter, P. Colestock, M. Light, E. A. Bering, III, T. W. Glover, C. Davis, and D. G. Chambers, *Bull. Am. Phys. Soc. DPP03*, RP1.138 (2003).
- ⁶⁶V. I. Krassovsky, *Proc. IRE* **47**, 289 (1959).
- ⁶⁷E. C. Whipple, *Proc. IRE* **47**, 2023 (1959).
- ⁶⁸L. W. Parker and E. C. Whipple, *J. Geophys. Res.* **75**, 4720, doi:10.1029/JA075i025p04720 (1970).
- ⁶⁹W. B. Hanson, R. A. Heelis, R. A. Power, C. R. Lippincott, D. R. Zuccaro, B. J. Holt, L. H. Harmon, and S. Sanatani, *Space Sci. Instrum.* **5**, 503 (1981).
- ⁷⁰S. Minami and Y. Takeya, *J. Geophys. Res.* **87**, 713, doi:10.1029/JA087iA02p00713 (1982).
- ⁷¹J. P. Squire, F. R. Chang Díaz, R. Bengtson, J. R. Bussell, V. T. Jacobson, A. J. Wooton, E. A. Bering III, T. Jack, and A. Rabeau, *Bull. Am. Phys. Soc. DPP97*, pThp.M2.02 (1997).
- ⁷²S.-L. Chen and T. Sekiguchi, *J. Appl. Phys.* **36**, 2363 (1965).
- ⁷³M. Light, personal communication (2003).
- ⁷⁴I. H. Hutchinson, *Principles of Plasma Diagnostics* (Cambridge University Press, Cambridge, 1987).
- ⁷⁵R. L. Stenzel, R. Williams, R. Aguero, K. Kitazaki, A. Ling, T. McDonald, and J. Spitzer, *Rev. Sci. Instrum.* **53**, 1027 (1982).
- ⁷⁶R. L. Stenzel, W. Gekelman, N. Wild, J. M. Urrutia, and D. Whelan, *Rev. Sci. Instrum.* **54**, 1302 (1983).
- ⁷⁷M. D. Carter, F. W. J. Baity, G. C. Barber, R. H. Goulding, Y. Mori, D. O. Sparks, K. F. White, E. F. Jaeger, F. R. Chang Díaz, and J. P. Squire, *Phys. Plasmas* **9**, 5097 (2002).
- ⁷⁸W. B. Hanson and D. D. McKibbin, *J. Geophys. Res.* **66**, 1667, doi:10.1029/JZ066i006p01667 (1961).
- ⁷⁹W. B. Hanson, S. Sanatani, D. Zuccaro, and T. W. Flowerday, *J. Geophys. Res.* **75**, 5483, doi:10.1029/JA075i028p05483 (1970).
- ⁸⁰R. E. Bourdeau, E. C. Whipple, J. L. Donley, and S. J. Bauer, *J. Geophys. Res.* **67**, 467, doi:10.1029/JZ067i002p00467 (1962).
- ⁸¹R. E. Bourdeau and J. L. Donley, *Proc. R. Soc. London, Ser. A* **281**, 487 (1964).
- ⁸²B. W. Longmier, A. D. Gallimore, F. R. Chang Díaz, J. P. Squire, T. W. Glover, D. G. Chavers, I. Bering, E. A. Bering III, and B. M. Reid, *J. Propul. Power* **25**, 746 (2009).
- ⁸³C. T. Dum and T. H. Dupree, *Phys. Fluids* **13**, 2064 (1970).